ADVANCED ENERGY MATERIALS
www.advenergymat.de

# Visualizing Performances Losses of Perovskite Solar Cells and Modules: From Laboratory to Industrial Scales

*Genghua Yan, Ye Yuan,* Mory Kaba, and Thomas Kirchartz**

**While the efficiencies of lab-sized perovskite solar cells are continuously rising, a variety of challenges have to be overcome to realize remotely similar efficiencies in an industrial context. Any changes in the preparation process, device size, device architecture, and material type are likely to result in efficiency loss. To date, there have been no solutions that can produce large-area modules with performance comparable to that of laboratory devices. However, depending on the type of deposition process, the dominant loss mechanisms differ significantly, which can guide the further optimization of processes and devices. In this study, a meta-analysis of state-of-the-art perovskite solar cells and modules with different preparation methods, area sizes, and material compositions, is presented. Moreover, the efficiency losses are divided into five figures of merit and they are visualized to discuss the efficiency-limiting loss mechanisms that must be overcome for commercialization.**

## 1. Introduction

Perovskite solar cells have been developed for over a decade, with peak power-conversion efficiencies exceeding 26%,[1] which is approaching that of silicon solar cells, as well as higher than that of all single-junction commercial photovoltaic modules, including silicon, cadmium telluride (CdTe), and copper indium gallium selenide (CIGS) modules.[2] Therefore, the next hotspot for the halide perovskite research community is technology transfer from laboratory to industrial applications. However, the manufacturing of efficient and stable solar cells and modules in larger areas is challenging for metal-halide perovskites because of their sensitivity to heat, oxygen, moisture, and UV radiation. Furthermore, the upscaling of processes developed for small areas requires the transfer of processes to scalable preparation methods. Thus far, spin-coating is still the most widely used preparation method in laboratories; all devices with efficiencies greater than 25% have been prepared using spin-coating (with one notable exception so far[3]). However, spin-coating is unsuitable for upscaling printed large-area photovoltaics. The typically considered technologies that are applicable to printable photovoltaics include blade coating, slot-die coating, inkjet printing, screen printing, and spray coating.[4] While one of the key unique selling points for laboratory research on halide perovskites is the ability to use solution processing (printing or coating methods), vacuum evaporation is considered for perovskites in both smaller and larger areas. Vacuum evaporation can produce homogeneous and pinhole-free perovskite films and has the inherent advantage of enabling the deposition of high-quality thin films on textured silicon substrates.[5] Additionally, it is compatible with existing thin-film photovoltaic manufacturing lines.[6] Vacuum evaporation is a proven process for large-area thin-film solar modules such as those made from CdTe and Cu(In,Ga)$Se_2$.[6] Perovskites evaporated using vacuum processes are free of solvents and solution synthesis processes, which is the biggest difference from spin-coating. One of the most significant limitations of the vacuum process is the high cost. However, this could be mitigated by increasing the evaporation rate. By raising the rate to ≥720 nm $min^{-1}$ and number of linear sources to ≥10, the cost of vacuum evaporation can be reduced to a level comparable to the solution process, which is considered industrially achievable.[6,7] In fact, the commercial sector generally holds a positive outlook toward the future of vacuum technology in perovskite commercialization. According to Abzieher et al., ≈40% of perovskite module manufacturers and 70% of equipment manufacturers have indicated that they engage in vapor-phase deposition.[6] Furthermore, most of these manufacturers have well-established photovoltaic operations.[6] In contrast, companies that are announcing their engagement in printing methods tend to be emerging organizations.[6] However, printing processes have gained significant attention in the academic community and have become the subject of extensive research. The printing methods do not rely on high-speed rotation, which means that the solvent volatilization rate of the wet film is much lower than that of the spin-coating process. Such a low solvent volatilization rate affects the quality

---

G. Yan, Y. Yuan, M. Kaba, T. Kirchartz
IMD3-Photovoltaik
Forschungszentrum Jülich
52425 Jülich, Germany
E-mail: y.yuan@fz-juelich.de; t.kirchartz@fz-juelich.de
T. Kirchartz
Faculty of Engineering and CENIDE
University of Duisburg-Essen
Carl-Benz-Str. 199, 47057 Duisburg, Germany

The ORCID identification number(s) for the author(s) of this article can be found under https://doi.org/10.1002/aenm.202403706

**DOI: 10.1002/aenm.202403706**

of the perovskite film, especially for thick films. In addition, the requirements for the precursor solution are also different; that is, different methods require different solution properties, such as viscosity, concentration, surface tension, and contact angle.[4a,b] Any change in the type of solvent or ink properties increases the risk of introducing defects or changing the film formation. Overall, the experience gained from the spin-coating process is not entirely applicable to new methods. Currently, only a few studies have reported a champion efficiency of over 24% using preparation methods other than spin-coating.[3,8]

To date, all devices with efficiency >24% have been based on lab-scale areas (≤1 cm$^2$), and the efficiency decreases rapidly with increasing area. Single devices with larger areas have not been widely reported and have exhibited unsatisfactory performance. Nevertheless, perovskite modules with areas between 10 and 70 cm$^2$ have been developed and reported in recent years. However, for modules with larger areas (≥100 cm$^2$), only a few studies have been published.[8b] In addition to encouraging progress in the academic community, manufacturers have made remarkable achievements. Perovskite module records were reported by SolarEon Technology Co., Ltd. (19.2%, 1027 cm$^2$) and Singfilm Solar (22.6%, 20.25 cm$^2$). Unfortunately, no details were published, rendering the results unsuitable for further analysis in the context of the present study. There are several challenges during the upscaling procedure, including nonuniform film thickness and quality, single-device interconnection, increased series resistance, imperfect scribing, and laser etching processes (which may result in film damage and residues).[4b,9] These problems result in efficiency loss.

Perovskite materials face stability issues during their development. The intrinsic instabilities (e.g., organic contents and crystal-phase transition), as well as extrinsic factors (e.g., moisture, elevated temperature, continuous illumination, and bias voltage), cause the decomposition of perovskite absorbers and degradation of related devices,[10] which can be further attributed to an undesirable Goldschmidt tolerance factor, degradation of the organic components of the device, ion migration, and defects.[10a,11] To improve stability, approaches for defect passivation, substituting organic cations, and water and oxygen barriers have been investigated. It has been reported that light- and heat-induced degradation are related to defects.[12] Therefore, defect passivation can improve not only the efficiency but also the stability of perovskite solar cells. In addition, all-inorganic and quasi-2D perovskites have attracted considerable attention as potential alternatives to hybrid 3D perovskites. By substituting organic components with inorganic ones, all-inorganic perovskites exhibit better thermal stability than perovskites with organic A-site cations.[13] They can sustain a temperature that is higher than the conventional perovskite encapsulation temperature (≈140 °C) and device operating temperature (≈85 °C).[4b,14] Quasi-2D perovskites exhibit excellent moisture stability owing to the introduction of hydrophobic bulky organic cations.[15] Meanwhile, quasi-2D perovskites also possess small nonradiative recombination losses, strong van der Waals interactions, and high formation energy.[15a] Nevertheless, as emerging materials, the efficiency of solar cells based on all-inorganic and quasi-2D perovskites is still not comparable to that of their hybrid halide counterparts. Therefore, understanding the distribution of energy loss is important for further development.

In summary, many factors cause efficiency losses that can significantly increase when scaling up to larger areas and when using roll-to-roll compatible printing methods. These efficiency losses must be thoroughly understood and reduced before commercialization. As shown in this article, the dominant loss mechanisms vary depending on the deposition process and the exact absorber composition. Therefore, it is important to quantify different losses and understand their corresponding physical mechanisms. In this study, we systematically present a meta-analysis of state-of-the-art perovskite solar cells and modules with different preparation processes, area sizes, and compositions. Moreover, we analyzed the physical mechanism corresponding to the losses by breaking them down into several figures of merit (FoMs) representing the photocurrent, resistive, and recombination losses.

## 2. Theoretical Methodology

In **Table 1**, we summarize the core equations for the FoMs and the corresponding physical loss mechanisms used for loss analysis. The basic parameters of the cell are included in these FoMs. In Equation (1), the relationships between $\eta$, $V_{\text{oc}}$, $J_{\text{sc}}$, and $FF$ are described, and the efficiency loss is broken down into five FoMs, indicating the short-circuit current density, fill factor, and open-circuit voltage losses separately. The $F_{\text{sc}}$ term in Equation (3) reflects the photocurrent loss owing to photons that have not been effectively absorbed and converted. Equation (2) expresses the fill factor under ideal conditions (i.e., without series resistance and with infinite parallel resistance). Generally, the fill factor slightly increases with $V_{\text{oc}}$, which is illustrated by the $F_{\text{FF}}^{V_{\text{OC}}}$ from Equation (4), and is typically a small loss for all studied cases. However, because the resistive losses and nonunity ideality factors were not considered in Equations (2) and (4), the measured fill factor (regarded as $FF^{\text{real}}$) would be lower than $FF_0(V_{\text{OC}}^{\text{real}})$. This $FF$ loss is reflected in the figure of merit $F_{\text{FF}}^{\text{res}}$ in Equation (5). Moreover, there are three open-circuit voltages in the equations: the actual open-circuit voltage $V_{\text{OC}}^{\text{real}}$ of a real device, the open-circuit voltage $V_{\text{OC}}^{\text{rad}}$ in the radiative limit, and the open-circuit voltage $V_{\text{OC}}^{\text{SQ}}$ in the SQ model (i.e., radiative limit combined with a step-function-like absorption). The calculation method of $V_{\text{OC}}^{\text{rad}}$ was elaborated in detail by Krückemeier et al.[16] The factor $F_{\text{OC}}^{\text{nonrad}}$ considers the nonradiative recombination loss, whereas $F_{\text{OC}}^{\text{rad}}$ is a measure of the abruptness of the absorption edge. Thus, the more the absorptance resembles a step function, the closer to unity the $F_{\text{OC}}^{\text{rad}}$ will be. Equations (8)–(10) exhibit the calculation methods for the voltage loss. The total voltage loss $\Delta V_{\text{oc}}$ can be divided into two parts: the radiative recombination loss $\Delta V_{\text{OC}}^{\text{rad}}$ and the nonradiative recombination loss $\Delta V_{\text{OC}}^{\text{nonrad}}$. Similar to $F_{\text{OC}}^{\text{nonrad}}$, the voltage loss $\Delta V_{\text{OC}}^{\text{nonrad}}$ depends on the density of defects and the charge-carrier lifetimes. Moreover, we discuss the operational stability of perovskite solar cells. To evaluate the stability, we adopt $E_{\Delta\tau}$ ($\Delta\tau = 1000$ h) as an indicator, which has been described in Equation (11).[17] Currently, highly stable perovskite solar cells can achieve an $E_{1000\text{h}}$ of >20 Wh cm$^{-2}$.[17]

Using the equations listed in Table 1, we can analyze the efficiency-loss distribution of photovoltaic cells and modules. As shown in **Figure 1a**, the efficiency of lab-scale perovskite cells (26.7%)[2] has reached third place in the group of single-junction cells and its normalized efficiency $\eta^{\text{real}}/\eta^{\text{SQ}}$ (84.09%) is

**Table 1.** SQ model equations, figures of merit (FoMs), operational stability test energy yield, corresponding description, and labeled colors in the figures.[16,18]

| No. | Equation | Description | Label |
|---|---|---|---|
| (1) | $\frac{\eta^{\text{real}}}{\eta^{\text{SQ}}} = F_{\text{SC}} \frac{V_{\text{OC}}^{\text{real}}}{V_{\text{OC}}^{\text{rad}}} \frac{V_{\text{OC}}^{\text{rad}}}{V_{\text{OC}}^{\text{SQ}}} \frac{\text{FF}_0\left(V_{\text{OC}}^{\text{real}}\right)}{\text{FF}_0\left(V_{\text{OC}}^{\text{SQ}}\right)} F_{\text{FF}}^{\text{res}}$ | The SQ efficiency percentage is defined with the help of five FoMs. The $V_{\text{OC}}, J_{\text{SC}}$, and *FF* implicit in these FoMs. The calculation method of $V_{\text{OC}}^{\text{rad}}$ is shown by Krückemeier et al.[16] | N/A |
| (2) | $\text{FF}_0 = \frac{\frac{qV_{\text{OC}}}{kT_{\text{cell}}} - \ln\left(\frac{qV_{\text{OC}}}{kT_{\text{cell}}} + 0.72\right)}{\frac{qV_{\text{OC}}}{kT_{\text{cell}}} + 1}$ | Ideal fill factor value without any resistive losses and with $n_{\text{id}} = 1$. | N/A |
| (3) | $F_{\text{SC}} = J_{\text{SC}}/J_{\text{SC}}^{\text{SQ}}$ | FoM. Photocurrent loss. | 🟨 |
| (4) | $F_{\text{FF}}^{V_{\text{OC}}} = \text{FF}_0\left(V_{\text{OC}}^{\text{real}}\right)/\text{FF}_0\left(V_{\text{OC}}^{\text{SQ}}\right)$ | FoM. FF loss due to the loss in $V_{\text{oc}}$. | 🟪 |
| (5) | $F_{\text{FF}}^{\text{res}} = FF^{\text{real}}/FF_0\left(V_{\text{OC}}^{\text{real}}\right)$ | FoM. FF loss due to the series, parallel resistance. | 🟥 |
| (6) | $F_{\text{OC}}^{\text{nonrad}} = V_{\text{OC}}^{\text{real}}/V_{\text{OC}}^{\text{rad}}$ | FoM. Nonradiative recombination voltage loss. | 🟩 |
| (7) | $F_{\text{OC}}^{\text{rad}} = V_{\text{OC}}^{\text{rad}}/V_{\text{OC}}^{\text{SQ}}$ | FoM. Voltage loss due to discrepancy between the actual absorption coefficient and the assumed step-function. | 🟦 |
| (8) | $\Delta V_{\text{OC}} = V_{\text{OC}}^{\text{SQ}} - V_{\text{OC}}$ | Total voltage loss calculation method. | N/A |
| (9) | $\Delta V_{\text{OC}}^{\text{rad}} = V_{\text{OC}}^{\text{SQ}} - V_{\text{OC}}^{\text{rad}}$ | Radiative recombination voltage loss calculation method. | N/A |
| (10) | $\Delta V_{\text{OC}}^{\text{nonrad}} = \Delta V_{\text{OC}} - \Delta\, V_{\text{OC}}^{\text{rad}} = V_{\text{OC}}^{\text{rad}} - V_{\text{OC}}$ | Nonradiative recombination voltage loss calculation method. | N/A |
| (11) | $E_{\Delta\tau} = \int_0^{\Delta\tau} P_{\text{out}}\, dt = \int_0^{\Delta\tau} P_{\text{in}}\, \eta\, dt$ | Operational stability test energy yield $E_{\Delta\tau}$, which is used to quantify the stability of the device. $\Delta\tau$ is the duration time of the test, and here we fix $\Delta\tau = 1000$ h in this paper. $P_{\text{out}}$ and $P_{\text{in}}$ are the output and incoming power density, respectively. $\eta$ is the efficiency of the cell.[17] | N/A |

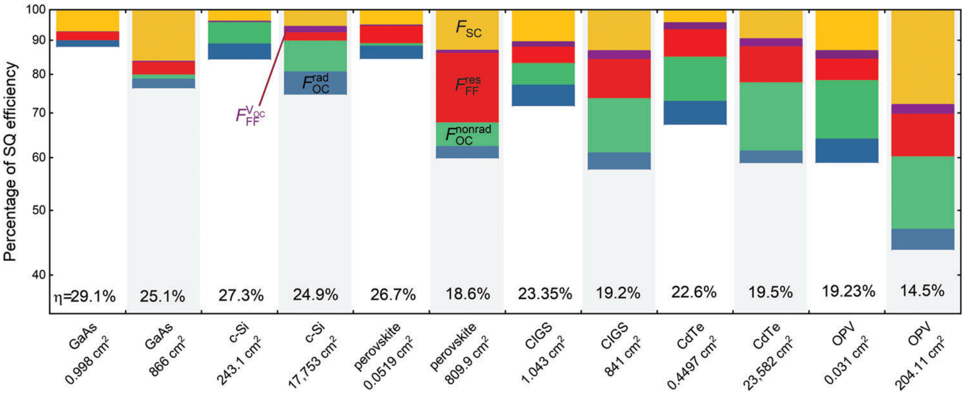

**Figure 1.** Comparison of losses for certified single-junction cells and modules. The light-colored background was used to represent the module samples. Note that the *y*-axis of the figures is plotted logarithmically to ensure that changing the order of the losses does not change the size of the bar segments. The perovskite module exhibits significant increases relative to the cell in all losses, especially in terms of $F_{\text{SC}}$, $F_{\text{FF}}^{\text{res}}$, and $F_{\text{OC}}^{\text{nonrad}}$. Please note that the efficiency record for perovskite modules has recently reached 19.2% for an area of 1072 cm$^2$ and 20.6% for a slightly smaller area of 215 cm$^2$. Furthermore, 19.9% was achieved for a CdTe module;[1a,b] however, detailed information (e.g., EQE spectra, number of subcells) have not yet been published, and thus, we cannot calculate the corresponding figures of merit.

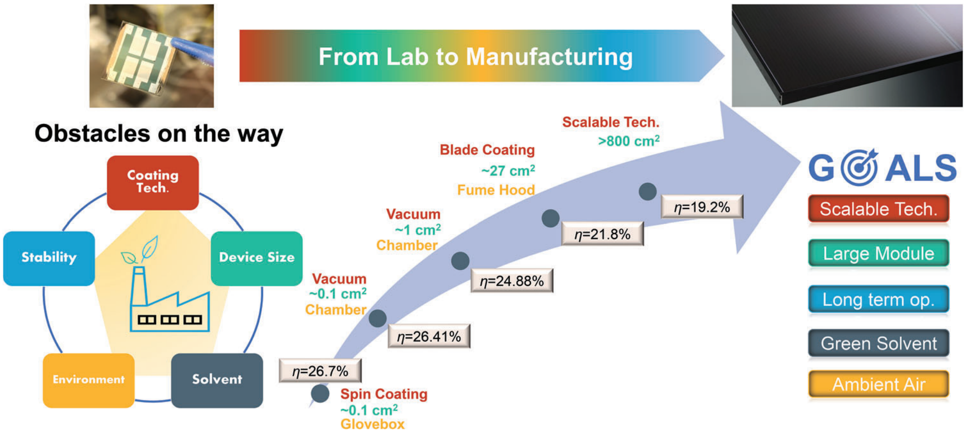

**Figure 2.** Evolution of the efficiency $\eta$ for perovskite solar cells and modules toward commercialization and the corresponding key influencing factors.

even slightly higher than crystalline silicon (83.94%) and only marginally lower than that of GaAs (87.69%). However, as a module with an area >800 cm$^2$, its efficiency (≈19%) and $\eta^{\text{real}}/\eta^{\text{SQ}}$-ratio (≈60%) are far behind those of GaAs and c-Si modules. All losses increased during the upscaling process of halide perovskites. Compared with the most successful commercial c-Si modules, perovskite modules are far behind in terms of $F_{\text{SC}}$, $F_{\text{FF}}^{\text{res}}$, and module area.

There are several obstacles to the commercialization of perovskite photovoltaics, including module manufacturing, scalable perovskite preparation, film/device stability, the substitution of toxic solvents, and ambient-air preparation. **Figure** 2 shows the efficiency evolution for each key step based on the current state-of-the-art. Among these issues, the first three goals are the most important, and can directly determine the chances of successfully commercializing perovskite modules. In this study, we focus on three aspects: the cell and module area, scalable preparation method, and stability, and illustrate the development of efficiency losses as a function of these additional constraints.

## 3. Perovskite Preparation Processes

### 3.1. Meta-Analysis

**Figure** 3 shows the performance of high-efficiency perovskite solar cells prepared using different preparation methods for the perovskite absorber layer. We analyzed and discussed the devices with the highest efficiency (at least $\eta \geq 18\%$) for each category. We adopted a unified inflection point method to acquire the bandgap $E_{\text{g}}^{\text{ip}}$ of each device;[16,18c] thus, all the data points in the figure are based on such a unified bandgap calculation method. Note that we were unable to consider publications that did not report the external quantum efficiency spectra. Spin-coated perovskite solar cells generally show the highest efficiencies among all processing methods. The best certified efficiency is ≈26.7%, and many groups have reported devices with champion efficiencies $\eta \geq 25\%$.[3,19] The values of $J_{\text{SC}}$, $V_{\text{OC}}$, and $FF$ are very good and higher than those of other methods. In recent years, vacuum-prepared devices have undergone significant advancements in terms of their efficiency. Prior to 2022, the champion efficiency was ≈20.5%.[20] In 2022, this efficiency rose to ≈24.4% on a scale of 0.1 cm$^2$.[8a] In 2024, a new recorded efficiency of 26.41% (with certified value of 26.21%) was reported on a 0.1 cm$^2$ scale, along with a certified value of 24.88% on a 1 cm$^2$ scale.[3] Among all printing methods, the blade coating process shows the highest efficiency. An efficiency $\eta = 24.6\%$ (0.08 cm$^2$) was achieved with blade coating in 2023, followed by slot-die coating (23.4%),[21] R2R-compatible blade coating (21.76% for flexible devices),[22] inkjet printing (21.6%),[23] screen printing (20.52%),[24] and spray coating (19.6%).[25]

As the bandgap energy differs from device to device, simple performance indicators are not sufficient to make a fair comparison between different devices within the lead-halide perovskite material family. Therefore, we calculated the fraction of each performance indicator relative to the value in the SQ-model for the given bandgap, as shown in **Figure** 4. The spin-coated devices exhibited the highest ratios, with $\eta/\eta^{\text{SQ}}$ >80%, $J_{\text{SC}}/J_{\text{SC}}^{\text{SQ}}$ ≈95%, and $V_{\text{OC}}/V_{\text{OC}}^{\text{SQ}}$, $FF/FF^{\text{SQ}}$ between 90% and 95%, which are the targets for other methods. Furthermore, we calculated the nonradiative recombination voltage loss $\Delta V_{\text{OC}}^{\text{nonrad}}$ using the method presented by Krückemeier et al.[16] and plotted it along with the bandgap $E_{\text{g}}^{\text{ip}}$ and $J_{\text{SC}}/J_{\text{SC}}^{\text{SQ}}$ (shown in **Figure** 5). The voltage loss $\Delta V_{\text{OC}}^{\text{nonrad}}$ correlates with the defect density of the film. Figure 5 shows that spin-coated samples can easily achieve ultralow voltage losses $\Delta V_{\text{OC}}^{\text{nonrad}} \leq 50$ mV, which means that solution-based defect passivation techniques are already mature and defects are no longer the main barrier for further development of the top spin-coated perovskite solar cells. The vacuum process is in second place and has achieved a champion $\eta/\eta^{\text{SQ}}$ of ≈83.60%. However, only two groups achieved $\eta/\eta^{\text{SQ}} > 70\%$, and all reports from the other groups were lower than 70%. Vacuum-processed devices typically exhibit good $J_{\text{SC}}/J_{\text{SQ}}$, but $V_{\text{OC}}/V_{\text{OC}}^{\text{SQ}}$ and $FF/FF^{\text{SQ}}$ fall behind the spin-coated samples. As illustrated in Figure 5, only one cell showed a comparable $\Delta V_{\text{OC}}^{\text{nonrad}}$ to that of the spin-coated sample, whereas the remaining cells displayed a significant $\Delta V_{\text{OC}}^{\text{nonrad}}$ loss, with >50% of samples having a loss of more than 100 mV. Although the vacuum method can produce homogeneous and pinhole-free thick films, which is advantageous for achieving a high short-circuit current density, the corresponding crystallization control and nonsolution passivation process are more

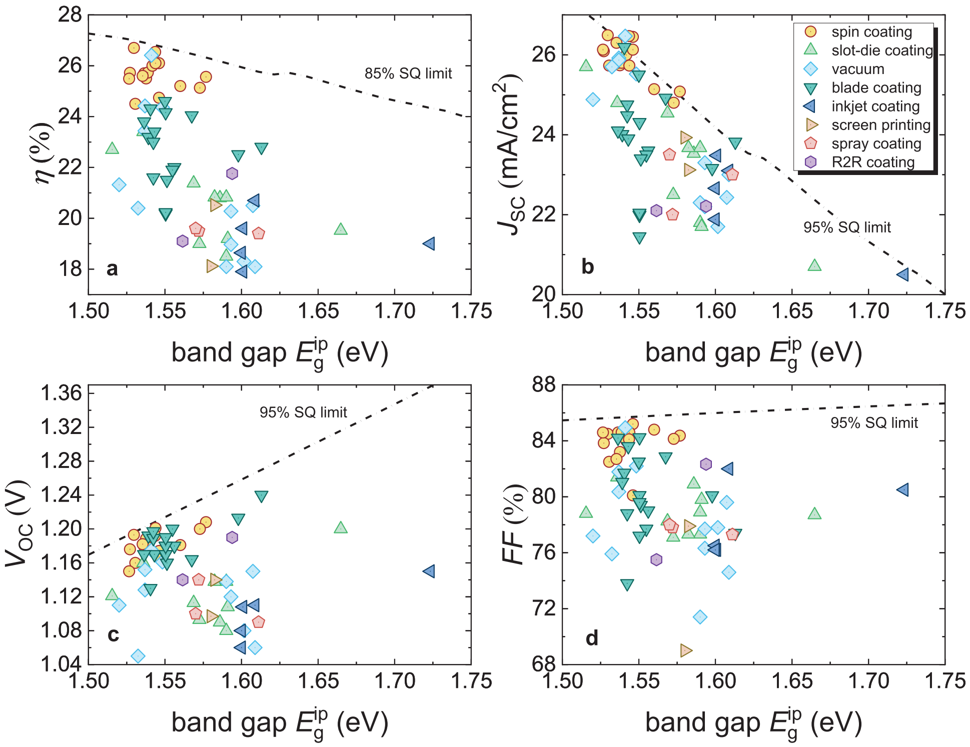

**Figure 3.** Performance of small-area perovskite solar cells as a function of bandgap and perovskite preparation processes as color-coded parameters. a) Efficiency, b) short-circuit current density, c) open-circuit voltage, and d) fill factor. Spin-coated perovskite solar cell exhibited the highest efficiency of 26.7%,[2] followed by vacuum (26.41%),[3] blade coating (24.6%),[8c] slot-die coating (23.4%),[21] R2R-compatible blade coating (21.76%),[22] inkjet printing (21.6%),[23] screen printing (20.52%),[24] and spray coating (19.6%).[25]

challenging to implement than the spin-coating technique.[26] The blade coating process yielded a high $\eta/\eta^{SQ}$ of ≈78.29%. For the slot-die coating, a champion $\eta/\eta^{SQ}$ of ≈74.08% was achieved with a medium fraction of the performance parameters relative to their respective values in the SQ model. The preparation mechanisms for slot-die coating and blade coating are similar; both are based on the concave meniscus caused by the surface tension of the liquid. The main difference between the setups is the supply of perovskite ink. The slot-die coating has a specialized slot die head for a more precise ink supply control.[4a,b] Both slot-die and blading coatings are quite different from spin-coating; in particular, they do not have a rapidly rotating substrate, which means that the rate of transformation from wet to dry films is quite slow. The solvent volatilization step is very important for the film quality, especially for thick films. To overcome this problem, the setups for both the slot-die coating and blade coating processes are typically equipped with an air-blowing component to accelerate the volatilization of the solvent in the film. However, from our meta-analysis, we find that using such equipment is still insufficient to obtain film quality that is as good as that of the spin-coated one. Another approach is to reduce the thickness of the film; however, this certainly reduces the short-circuit current density. Figure 5 shows that many blade-coated and slot-die-coated samples generally exhibit an obvious trade-off relationship between $\Delta V_{OC}^{nonrad}$ and $J_{SC}/J_{SC}^{SQ}$. In addition, roll-to-roll (R2R) systems employ blade coating or slot-die coating techniques to fabricate perovskite films. Therefore, we observe that the R2R printed samples follow a similar trend. In Figures 4 and 5, two R2R printed samples are recorded, both of which exhibit $J_{SC}/J_{SC}^{SQ}$ ≈90% and $\Delta V_{OC}^{nonrad} > 100$ mV. The best $\eta/\eta^{SQ}$ was ≈70.88%. The other three preparation processes recorded in the figure are inkjet printing, screen printing, and spray coating. The best values for $\eta/\eta^{SQ}$ for each preparation process were ≈68.30%, ≈66.43%, and 64.01%, respectively. Meanwhile, they all exhibit a low $V_{OC}/V_{OC}^{SQ}$ ratio, but $J_{SC}/J_{SC}^{SQ}$ can exceed 90%. Additionally, these samples show high $\Delta V_{OC}^{nonrad}$ values >100 mV, which may be due to the induced defects (non-radiative recombination centers) during the precursor solution preparation process. A common feature of these three processes is the perovskite precursor solution (or ink or paste in some situations). The perovskite precursor solution used for spin-coating cannot be directly applied to these three processes because they have different requirements for the solution properties. For instance, a highly viscous perovskite ink is needed for inkjet and screen printing processes, whereas the spray coating process requires a solution with low surface tension and a small contact angle to ensure the coverage and uniformity of the perovskite film.[4a,b] Solution- and additive-engineering are widely used to adjust the solution properties. However, defects were thought to be introduced into the perovskite film as high-quality perovskite solutions are quite sensitive. Nevertheless, processes such as screen and inkjet printing can easily prepare thick films because of the high viscosity and concentration of the perovskite ink, which ensures a good $J_{SC}$ performance.

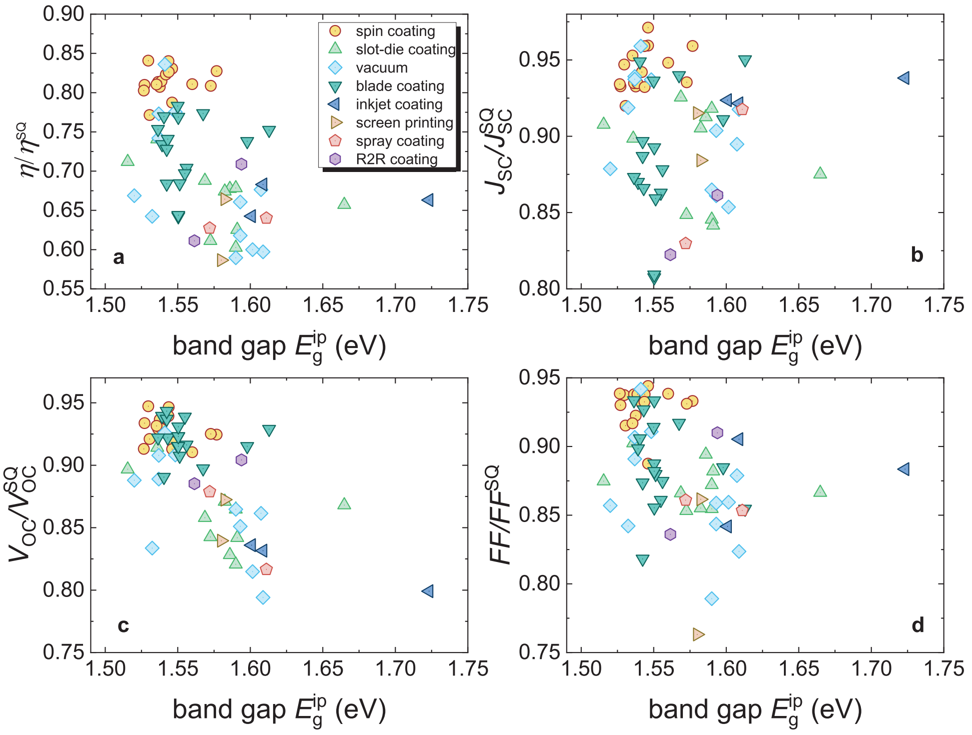

**Figure 4.** Performance as a fraction of the respective value in the SQ model for top-level perovskite solar cells for different perovskite preparation processes. a) $\eta/\eta^{SQ}$, b) $J_{SC}/J_{SC}^{SQ}$, c) $V_{OC}/V_{OC}^{SQ}$, and d) $FF/FF^{SQ}$. Spin-coated perovskite solar cell exhibited the highest $\eta/\eta^{SQ}$ of 84.09%,[2] followed by vacuum (83.60%),[3] blade coating (78.29%),[8c] slot-die coating (74.08%),[21] R2R-compatible blade coating (70.88%),[22] inkjet printing (68.30%),[23] screen printing (66.43%),[24] and spray coating (64.01%).[25] Currently, only the $J_{SC}/J_{SC}^{SQ}$ of the vacuum-prepared device and $V_{OC}/V_{OC}^{SQ}$ of the blade-coated device are comparable to those of the spin-coated devices.

Next, we use the FoMs listed in Table 1 to analyze the physical mechanisms behind the efficiency losses. First, we focused on highly efficient spin-coated devices. These devices serve as benchmarks for evaluating the performance of the other methods in this study. **Figure 6** shows the loss distribution of highly efficient spin-coated devices. The devices are categorized into two groups in terms of structure: regular and inverted. Inverted devices have demonstrated significant progress in recent years, with a 2% improvement in the certified efficiency from 2022 to 2024, surpassing 26%. This advancement is primarily attributed to the development of self-assembled monolayer-based hole-transport layers and interface engineering,[27] which has resulted in reduction in *FF* loss and current loss. Currently, devices with $\eta > 25\%$ exhibit a similar loss distribution for $J_{SC}$, *FF*, and $V_{OC}$, when comparing regular and inverted structures. In 2024, small-area flexible devices have also demonstrated significant advancements, with

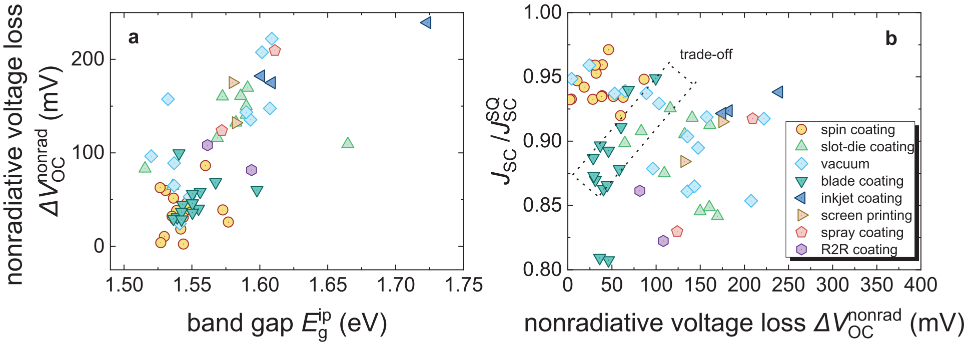

**Figure 5.** a) Distribution of nonradiative voltage loss $\Delta V_{OC}^{nonrad}$ along with $E_g^{ip}$. b) Performance distribution of nonradiative voltage loss $\Delta V_{OC}^{nonrad}$ versus $J_{SC}/J_{SC}^{SQ}$ for perovskite solar cells prepared by different processes. The square shows the trade-off relationship between the $\Delta V_{OC}^{nonrad}$ and $J_{SC}/J_{SC}^{SQ}$ for the blade coating and slot-die coating technologies. In addition, spin-coated devices can easily achieve an ultralow $\Delta V_{OC}^{nonrad} \leq 50$ mV, demonstrating the efficacy of the employed passivation techniques. Blade coating is the only scalable method that can yield a similar $\Delta V_{OC}^{nonrad}$.

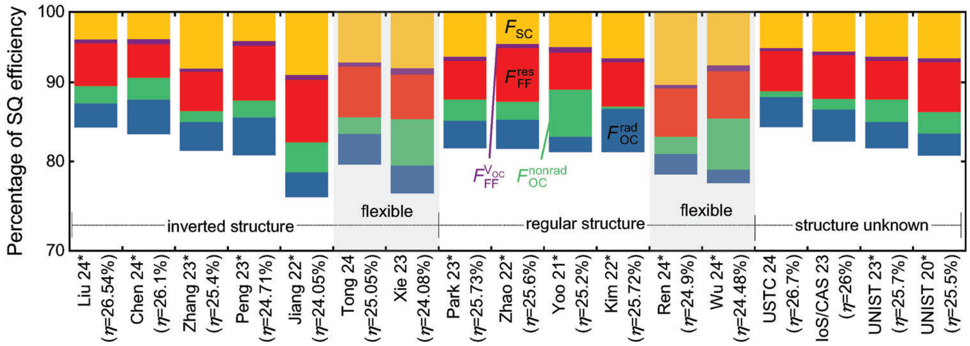

**Figure 6.** Visualized loss distribution for spin-coated perovskite solar cells with efficiencies >25%, as well as some representative flexible perovskite solar cells (indicated by light-colored background). The certified values are labeled with asterisks*. The others are reported champion values. Most of the devices showed large *FF* loss (red bars) and photocurrent loss (yellow bars) but small nonradiative recombination voltage loss (green bars). The inverted devices show significant efficiency improvement since 2023.

both regular and inverted devices achieving record efficiencies exceeding 25%.[28] Figure 6 presents several representative flexible devices, revealing that the efficiency loss is primarily concentrated on $F_{\mathrm{SC}}$ and $F_{\mathrm{OC}}^{\mathrm{nonrad}}$, compared to their rigid counterparts of the same type. After breaking down the $V_{\mathrm{OC}}$ loss into two parts, the results show that the voltage loss caused by nonradiative recombination (green bar) is lower than that caused by radiative recombination (blue bar) in most cases. As mentioned above, the nonradiative recombination losses in spin-coated devices are currently very low ($\Delta V_{\mathrm{OC}}^{\mathrm{nonrad}} \leq 50$ mV, as shown in Figure 5), and defects are no longer the primary efficiency-limiting factor. For lab-scale devices, the nonradiative voltage losses are already low. Thus, further efforts dedicated to further increase a small loss in lab-scale devices has a poor benefit/effort ratio. To further increase the open-circuit voltage, a potential starting point could be to reduce the radiative recombination losses, which correspond to the blue bar ($F_{\mathrm{OC}}^{\mathrm{rad}}$) in the figure. The factor $F_{\mathrm{OC}}^{\mathrm{rad}}$ is caused by the discrepancy between the actual absorptance and the assumed step function in the SQ model. In **Figure 7**, we display two EQE spectra with similar bandgaps and efficiencies but different $V_{\mathrm{OC}}$ loss distributions, which indicate that a smaller $F_{\mathrm{OC}}^{\mathrm{rad}}$ corresponds to a steeper absorption onset. Hence, exploring spectral modulation strategies to make the EQE edge closer to the step function will be helpful for further $V_{\mathrm{oc}}$ improvement. In addition, after separating the losses into five distinct parts, it is evident that the red ($F_{\mathrm{FF}}^{\mathrm{res}}$) and yellow ($F_{\mathrm{SC}}$) bars are typically the two components that constitute the largest fraction of the total losses. In the subsequent discussion, we will delve into the mitigation strategies in detail.

In **Figure 8**, we visualize the loss distribution of representative samples from all processes. The spin-coated samples are shown as references. These results are consistent with the discussion above. The vacuum samples show a similar small $F_{\mathrm{SC}}$ proportion to the spin-coated one, while the blade-coated samples show similar $F_{\mathrm{OC}}^{\mathrm{nonrad}}$ proportions. These results indicate the strengths of increasing the photocurrent and reducing the nonradiative recombination loss of the two methods, respectively. Additionally, the blade-coated, slot-die-coated, and R2R-fabricated flexible devices show a large $F_{\mathrm{SC}}$ loss or a trade-off relationship between $F_{\mathrm{SC}}$ and $F_{\mathrm{OC}}^{\mathrm{nonrad}}$, demonstrating the dilemma of balancing defects and film thickness. The inkjet-, screen-printing-, and spray-coating-prepared samples have a large $F_{\mathrm{OC}}^{\mathrm{nonrad}}$ proportion in most cases, which is consistent with the discussion about $\Delta V_{\mathrm{OC}}^{\mathrm{nonrad}}$. Moreover, the $F_{\mathrm{FF}}^{\mathrm{res}}$ part becomes the determining factor in many cases. Optimizing the series and parallel resistances can reduce the related losses. Nevertheless, the series resistance problem has not yet attracted much attention. Almost all reported devices are prepared on transparent conductive oxide (TCO) glass substrates. However, as an electrode, the electrical conductivity of TCO glass is far behind that of metal, which consequently results in losses owing to an increased series resistance. This type of loss is further magnified during upscaling. Optimizing the conductivity of the TCO and the transport layer, improving the carrier mobility, and designing the electrode architecture can reduce electrical loss. Subsequently, we further delve into the technologies of vacuum evaporation, blade coating, and slot-die coating. These technologies have experienced remarkable advancements in recent years, achieving promising efficiencies while concurrently displaying encouraging progress in the domain of large-area module manu-

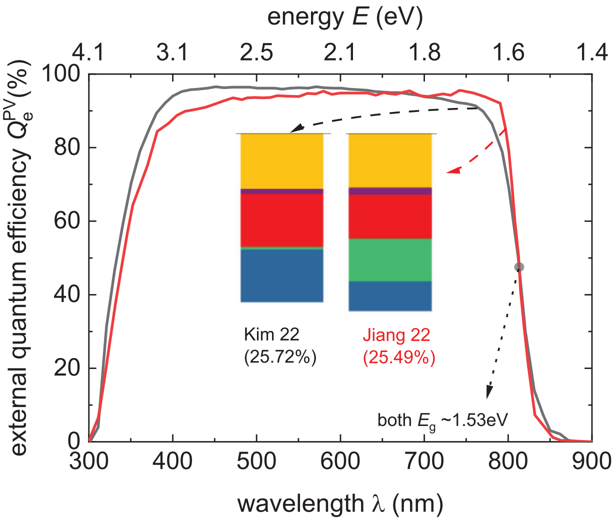

**Figure 7.** Comparison of EQE spectra for typical devices with different $F_{\mathrm{OC}}^{\mathrm{nonrad}}$ and $F_{\mathrm{OC}}^{\mathrm{rad}}$ losses. The spectra were reported by Kim et al.[19c] and Jiang et al.,[29] respectively. This result suggests that a smaller $F_{\mathrm{OC}}^{\mathrm{rad}}$ is correlated with a steeper absorption onset.

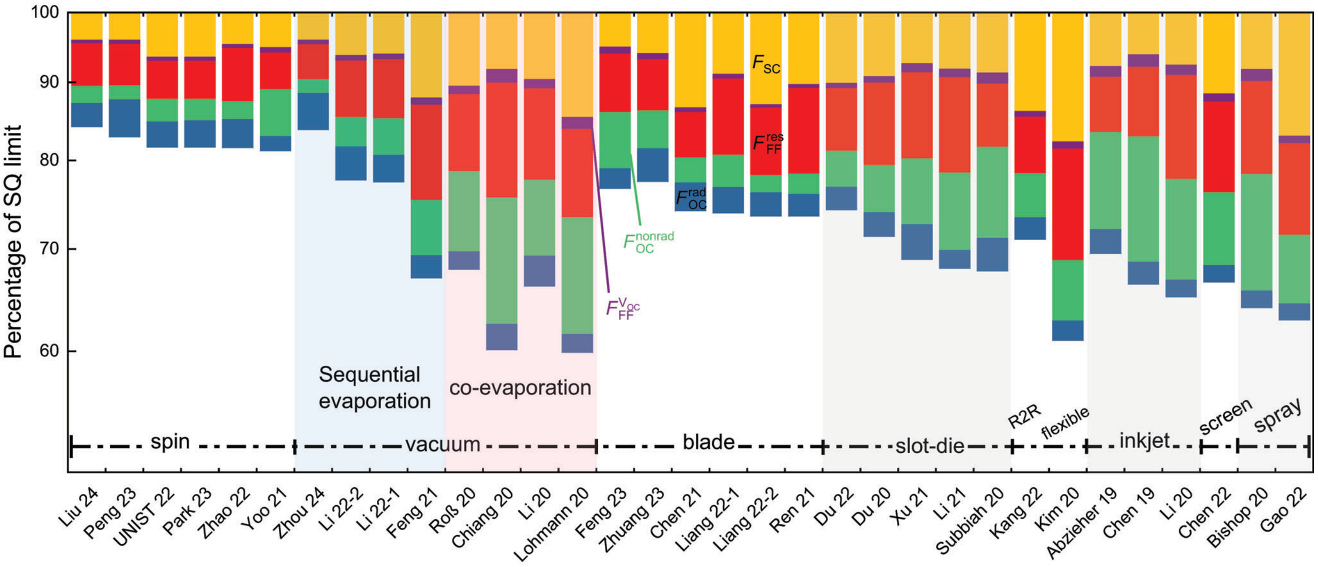

**Figure 8.** Visualized loss distribution for small-area perovskite solar cells prepared using different processes. A light-colored background was used to distinguish between the different processes. Among the scalable methods, the $F_{FF}^{res}$ part is the determining factor in many cases. In addition, the vacuum-prepared devices show a large $F_{OC}^{nonrad}$ loss, while the blade- and slot-die-coated devices show a large $F_{SC}$ loss or a trade-off relationship between $F_{SC}$ and $F_{OC}^{nonrad}$. However, the inkjet-, screen-printed, and spray-coated samples also have a large $F_{OC}^{nonrad}$ proportion.

facturing. Consequently, they are considered to be the most viable technologies for commercialization in the near future.

### 3.2. Progress of Vacuum Evaporated Perovskite Solar Cells

Over the last three years, evaporated perovskite solar cells have demonstrated significant advancements in terms of efficiency, which can be primarily attributed to the emergence of the sequential deposition technique. Prior to this, the codeposition technique was the prevailing method. When employing the codeposition technique, the quality of the film is typically regarded as the primary efficiency-limiting factor. Commonly, thin films exhibit small grains, poor crystallinity, and strong nonradiative recombination, as shown in the loss distribution graphs where the majority of green bars are quite large (Figure 8) as well as the corresponding nonradiative recombination voltage losses are predominantly above 100 meV (Figure 5).[26] During the codeposition process, both organic and inorganic substances are simultaneously vapor deposited. The evaporation of organic materials typically results in high vapor pressure, which impacts the functioning of quartz crystal monitors, leading to fluctuations in evaporation-rate detection and uncontrollable variations in film thickness.[6,30] Moreover, there is a risk of cross-contamination during the process, which could compromise the film quality. Fortunately, the situation has improved since 2021 as the sequential deposition technique, which separately evaporates organic and inorganic materials, has been developed and become more refined. For instance, Feng et al.,[30] Li et al.,[8a,31] and Zhou et al.,[3] employed the sequential deposition process and reported high-efficiency perovskite solar cells. As shown in Figure 8, their devices show a significant improvement in performance, particularly in the nonradiative recombination part (green part in the figure). Utilizing extensive experience in the field of solution processing is another factor contributing to the rapid progress observed in recent years. The solution methods widely incorporates chloride (Cl) into the process of film preparation to facilitate crystallization.[32] Li et al. successfully prepared a Cl-alloy-mediated precursor film by depositing $PbCl_2$ in combination with inorganic materials, namely, CsI and $PbI_2$, which improved the film's crystallinity and homogeneity.[8a] Additionally, methylammonium chloride (MACl) is commonly employed as an additive for solution process.[19g,32a,33] Drawing on such idea, Zhou et al. prepared a MACl layer in a sequential deposition, and the final device exhibited an efficiency as high as 26.2%.[3] It is evident that this type of learning from solution methods proves to be highly effective. However, very few instances have been reported to date. Numerous additives have proven successful in the solution process, such as alkyl ammonium chloride (RACl),[19g] propylammonium chloride (PACl),[19g] rubidium chloride (RbCl),[33] and 1,3-bis(diphenylphosphino)propane (DPPP, diphosphine Lewis base).[12c] Some of these additives exhibit synergistic effects. For instance, RACl has been shown to further enhance device performance when used in conjunction with MACl.[19g] However, these studies were confined to the domain of solution-based preparation, indicating that incorporating these additives into vacuum-compatible processes holds significant potential. Another primary factor contributing to the enhanced efficiency, particularly the diminished voltage losses, is the use of passivation technologies inspired by the solution methods. Both Zhou et al.[3] and Li et al.[8a] carried out surface passivation in their studies, which effectively reduced the nonradiative recombination losses to below 50 mV. Unfortunately, the passivation method employed is still a solution-based process, and the transport layers are prepared by a solution process. In the future, it will be crucial to investigate the vacuum-based preparation of the passivation and transport layers. Interrupting the vacuum process complicates the procedure and increases expenses, which is unacceptable in the manufacturing industry.[6] Nonetheless, the rapid development of the vapor deposition technology is a pleasant surprise.

In addition to the aforementioned points, there are three aspects that warrant consideration with respect to vacuum-evaporated devices. The first pertains to the absorber composition. Currently, most high-efficiency vapor-deposited devices use double-cation perovskites (Cs and FA cations)[3,8a,31] Although this composition has also proven to be effective for solution-based methods, a greater number of devices with efficiency >25% are based on more complicated compositions.[29,34] The second point is the device structure. At present, all devices with efficiencies greater than 21% adhere to regular structures (i.e., *n–i–p*). However, comparatively less effort has been directed toward the study of inverted structures (i.e., *p–i–n*). The last aspect is the thickness of the absorber. Although vacuum evaporation processes have the capability to yield high-quality thick films, this goal has not yet been achieved. The thickness of most samples is ≈500 nm so far.[6,20,35] The limiting factor for thick absorber layers is the low carrier extraction velocity of the corresponding transport layers. A thick absorber layer can generate more charge carriers than a thin one. If these photogenerated carriers cannot be efficiently extracted by the transport layers, they would accumulate at the interfaces, resulting in increased recombination for finite load resistances (i.e., for $V < V_{\mathrm{OC}}$). Consequently, both the *FF* and $V_{\mathrm{OC}}$ of the device will decrease.[6,36] In recent years, the thickness of the film has tended to increase to ≈600 nm along with the reduction of recombination loss (e.g., ≈650 nm;[3] ≈630 nm;[8a] ≈650 nm;[20] ≈600 nm;[37] ≈560 nm[30]). This explains why the photocurrent loss in the device decreased after 2021. However, such thicknesses are still not enough for perfect absorption of the incident sunlight,[6] and there is no significant advantage over the films prepared by the solution method. Thus, in addition to improving the quality of the film, it is beneficial to increase the thickness simultaneously, which would result in a further reduction in photocurrent loss. Another strategy is to explore transport layers with increased drift-diffusion velocity and mobility. This would not only enhance the *FF*, but could also decrease the photocurrent loss.[38] As mentioned earlier, the carrier extraction velocity of the transport layer is the predominant factor that restricts the development of devices with thick perovskite films.

### 3.3. Progress in Blade-Coated Perovskite Solar Cells

Unlike vacuum evaporation, blade coating has achieved good progress in both regular- and inverted-structure devices. Both structures can obtain high efficiency, reaching ≥75% of the SQ limit (see Figure S1, Supporting Information). In general, perovskite compositions with lower proportion of FA cation are employed in the blade coating process (as well as slot-die coating). This contrasts significantly with the high-efficiency spin-coated device, in which the ratio of FA cation often exceeds 90% of the total number of cations. The reasons for this distinction relate to the quality of the film and the use of dimethyl sulfoxide (DMSO). It is essential to incorporate a significant quantity of DMSO when coating high-quality FAI-containing perovskite thin films, as the formation of the FAI–$PbI_2$–DMSO intermediate phase is crucial for crystallization.[39] Nevertheless, DMSO possesses a high boiling point of 189 °C, rendering it challenging to volatilize the solvent during the blade coating process. As mentioned before, printing methods encounter the more severe problem of slow solvent volatilization when compared with spin-coating. Consequently, decreasing the DMSO content could make it easier to enhance film quality. Therefore, it is recommended to decrease the FAI content. Deng et al. demonstrated that utilizing only dimethylformamide (DMF) as the solvent, it was only when the value of $x$ was decreased to 0.4 that a blade-coated $FA_xMA_{1-x}PbI_3$ film with good coverage and film morphology was possible.[40]

The short-circuit current density serves as the predominant constraint for the bladed-coated devices. Figure S1 of the Supporting Information illustrates the performance distributions of regular and inverted devices. No significant differences were observed between these two structures. A small number of devices have $J_{\mathrm{SC}}/J_{\mathrm{SC}}^{\mathrm{SQ}}$ values approaching 95%, whereas the majority have values ≤90%. A possible reason for the lower short-circuit current density is the lower absorber thickness. By reducing the film thickness, more solvent can volatilize from the wet film, so that the issue of solvent residue would not be as serious as in thick films. As a matter of fact, many high-efficiency devices have a low thickness, typically ≤500 nm.[41] However, several studies have been conducted using absorber layers with thicknesses that are not excessively low. For instance, Fei et al., Liang et al., and Chen et al. have employed a thickness of ≈900 nm,[8c] ≈700 nm,[42] and ≈650 nm,[43] respectively, for the absorber layer. The loss distribution of these devices is displayed in Figure 8 (excluding Fei et al., because of the lack of an EQE spectrum). All the represented devices exhibited a large $F_{\mathrm{SC}}$ part, illustrating the existence of additional constraints beyond the thickness that must be considered. The issues of morphology and uniformity of the blade-coated films could be one of the reasons for the reduced short-circuit current density. In 2019, Mundt et al. utilized spatially resolved measurements to examine the surface of blade-coated perovskite films, revealing the presence of comet-shaped spots, blade-coated stripes, and overlaying patterns on the film surface.[44] These features alter the short-circuit current density distribution on the film surface, highlighting the importance of enhancing layer homogeneity for short-circuit current density improvement. Deng et al.[45] observed polygon domains on a scale of 20–100 µm and numerous concentric rings within these domains when using a substrate-heating process during blade coating. The polygon domains are primarily caused by Rayleigh–Bénard convection[46] during blading and are influenced by the temperature of the substrate, whereas the concentric rings are determined by the "coffee ring effect"[47] and are affected by the solution concentration. Owing to these concerns, it appears that Huang's group discontinued the use of the substrate heating process in their recent publications,[8c,39] despite its ability to facilitate solvent evaporation from the bottom of the film.

The issue of voids could be another possible reason for the reduced short-circuit current density. Numerous studies have observed a considerable number of pinholes on the surface of blade-coated films. Furthermore, Chen et al. demonstrated the presence of voids at the bottom of the film, the depth of which can reach up to 100 nm. Surface defects and amorphous-phase perovskites were observed surrounding the voids. Moreover, the presence of these voids can cause a split between the absorber and transport layers, thus influencing the carrier extraction efficiency of the transport layers. Additionally, poorly conductive compositions appeared around these voids after light illumination,[8c,39,48] which may increase the series resistance. Obviously, the voids have a significant impact on various device performance parameters, including stability, open-circuit voltage, fill factor, and short-circuit current density. These voids are believed to originate from the presence of high-boiling-point solvents such as DMSO in the wet films. The formation of perovskite films typically commences at the film–air interface,[49] resulting in the creation of a "shell" that traps DMSO at the bottom of the film. During the annealing process, there is a possibility that the DMSO may escape from the film, but it often leaves behind voids.[39] Chen et al. discovered that both $J_{SC}$ and FF decreased with an increase of DMSO content in the solution. However, as mentioned above, DMSO is crucial for perovskite film crystallization. A reduction in DMSO may also hinder the film performance. Hence, Chen et al. employed a solid-state lead-coordinating additive of carbohydrazide (CBH) to partially replace DMSO, which can reduce the voids and passivate the defects simultaneously. As a result, they obtained a cell with a certified stabilized $\eta$ of 23.6% and a module efficiency of 19.2% (aperture area 50.0 $cm^2$).[39] As shown in Figure 8, the device exhibited a small loss in open-circuit voltage and *FF*. In 2024, Fei et al. from the same team introduced a technique to effectively minimize the amorphous region at the base of perovskite films by incorporating lead-chelating molecules and bathocuproine into hole transport layers. They achieved certified efficiencies of 24.1% on device with area of 0.08 $cm^2$ and 21.8% on minimodules with an aperture area of 26.9 $cm^2$.[8c]

The aforementioned studies aimed to improve the perovskite film quality and mitigate the issues arising from voids, defects, and amorphous regions, while maintaining the use of DMSO. It is also possible to consider alternative approaches such as promoting the evaporation of solvents or replacing DMSO. Bu et al. developed a self-dying method that utilized DMF (boiling point = 153 °C) as the solvent along with *N*-methyl-2-pyrrolidone (NMP) and MACl, and regulated the phase-transition process to produce a pinhole-free compact perovskite film without the use of an antisolvent. Consequently, a champion efficiency of 15.3% with an aperture area of 205 $cm^2$ was reported for a module containing a blade-coated perovskite absorber, which corresponds to an efficiency of 15.83% with an effective area of 196.8 $cm^2$. It should be noted that NMP is a high-boiling point reagent (boiling point = 202 °C), and 96 µL of NMP was added to 500 µL of DMF. The issue of NMP volatilization has been addressed by reducing the film thickness; that is, the thickness of the spin-coated film was ≈700 nm, while the blade-coated film for the module was ≈550 nm.[8b] Therefore, the current loss increased during upscaling. Liang et al. employed a green and volatile solvent, ethanol (EtOH), into the perovskite ink to partially replace the conventional solvent, with the aim of enhancing both the film crystallization and device performance. As depicted in Figure 8, the device exhibited an exceptionally low nonradiative recombination loss, although the photocurrent losses remained relatively high.

In summary, over the past few years, a significant amount of effort has been dedicated to addressing the numerous challenges associated with high-boiling solvents, resulting in the development of a diverse range of strategies. However, most of these approaches have resulted in reduced nonradiative recombination losses without noticeable improvements in the short-circuit current density. Reducing the short-circuit current density loss has become a top priority for the next step in the development of blade-coated perovskite solar cells and modules.

### 3.4. Progress in Slot-Die Coated Perovskite Solar Cells

Slot-die coating presents notable benefits in terms of throughput, material utilization, and scalability, and it can be seamlessly integrated into industrial sheet-to-sheet and roll-to-roll systems.[50] It is a highly beneficial process that can be employed on a large scale. Slot-die coating entails a film preparation process and principle, which is similar to blade coating. The primary distinction lies in the use of a specialized slot-die head for more precise ink supply control. The development of slot-die technology emerged later than that of blade coating, which may be due to the complexity of the equipment. As shown in Figure 4, most slot-die-coated devices reached only ≈70% of their SQ limit. In addition to the high short-circuit current loss, the slot-die-coated devices also exhibited significant open-circuit voltage and *FF* losses. In terms of composition, numerous top-performing devices still rely on $MAPbI_3$ films. This is because the crystallization process of $MAPbI_3$ film does not rely heavily on DMSO, allowing for the reduction of high-boiling-point solvent usage. However, to improve the efficiency, it is necessary to gradually increase the proportion of formamidinium (FA) in the cations rather than pure methylamine (MA).[39,51] This stage has already been achieved by relevant studies on blade coating. In contrast to the blade-coating process, high-performance slot-die-coated devices have been primarily based on inverted structures so far. Nevertheless, this does not imply that normal structure will not be successful. In 2020, Du et al. developed a normal structure device that achieved an efficiency of 22.7% (71.20% of its SQ limit, shown in Figure 8).[52] These observations highlight the slower development of slot-die coating process compared with blade-coating process. Figure 8 shows the loss distribution of the top slot-die-coated devices reported in recent years. Subsequently, we examine the significant developments and advancements in this field based on these reports.

In recent years, extensive research has been conducted on replacing traditional solvents with low-boiling-point solvents for the slot-die coating process, similar to the efforts made in the field of blade coating. For instance, Subbiah et al. replaced the conventional DMF solvent with acetonitrile (ACN), a low-boiling-point solvent (82 °C), for the preparation of $MAPbI_3$ film, resulting in a significant improvement of solvent residue issue and enabling the film thickness to reach to µm level.[50] Figure 8 shows that the device exhibited a lower current density loss but a higher nonradiative recombination loss. The use of ACN was also reported by Xu et al., who have prepared micrometer-thick perovskite film by mixing MA and ACN as solvents. Additionally, they used a potassium thiocyanate additive to enlarge the grains,[53] leading to a decrease in the nonradiative recombination loss (as shown in Figure 8). Unfortunately, the losses in the *FF* part increased compared with the performance of Subbiah et al., and thus exhibited a similar efficiency level. Li et al. employed 2-methoxyethanol (2-ME, boiling point = 124 °C) as the solvent for $MAPbI_3$ films, and obtained micrometer-thick perovskite film as well. Furthermore, they added 12 mol% of DMSO to the solution to optimize the crystallization of the films.[54] It is anticipated that the films possess significant nonradiative recombination losses after the use of DMSO as shown in Figure 8. In the three studies mentioned above, the thickness of the $MAPbI_3$ perovskite film reached the micrometer level, resulting in a lower short-circuit current density loss. However, ensuring film quality and crystallization in thick films proved to be more challenging. Consequently, all three devices exhibited higher nonradiative recombination losses. Additionally, the carrier extraction ability of the transport layers is limited, which becomes the limiting factor for the $FF$ in thick films. Therefore, it is evident that all three devices experienced a larger percentage of $FF$ loss.

Enhancing the air knife process to expedite solvent volatilization is a conceivable strategy. Du et al. elevated the nitrogen pressure from 0.04–0.6 to 1.0 MPa, which led to an increase in high-speed nitrogen flow, facilitating the volatilization of solvents in the wet coating, and resulting in a rapid decline of film surface temperature. Such decreased temperature caused an oversaturation of the solution, and thus optimized the crystallization.[52] As evidenced in Figure 8, the device performance approached ≈70% of the SQ limit, and the loss distribution was relatively balanced. Du et al. proposed an alternative approach in 2022. They discovered that local dewetting and spontaneous shrinkage occurred during the printing process, resulting in the formation of numerous clusters and large exposed regions. They attributed this to the limited wettability of the substrate. Hence, they used electron-beam evaporated $NiO_x$ as the transport layer and employed surface redox engineering to improve the substrate wettability for the ink, which significantly increased the film coverage and resulted in high device performance (23.4% PCE and 74% SQ limit).[21] As demonstrated in Figure 8, their performance is in a leading position among their peers. The efficiency loss is dominated by the short-circuit current density loss, which is similar to that of blade-coated devices. It is worth mentioning that the stoichiometric ratio of perovskite used by Du et al. had a high percentage of FA among the cations. Thus, the lower bandgap is also responsible for its higher efficiency.

In summary, the development of slot-die technology followed the footsteps of blade coating. The focus of research has been on solving the problems caused by solvent volatilization. In recent years, significant progress has been made in improving the nonradiative recombination loss. It can be foreseen that the photocurrent density loss will primarily dominate the performance. In addition, research has concentrated on relatively high-bandgap $MAPbI_3$ thin films; however, additional research on low-bandgap perovskites is warranted in the future.

## 4. Upscaling Area Sizes

The additional loss during the upscaling process originates from two factors. 1) The preparation of large devices challenges the stability of the technology, including film uniformity and defect control. The uneven thickness affects $J_{SC}$, whereas the defect density affects $V_{OC}$.[4b] The problem of high TCO resistance during upscaling also results in an increase in $R_s$ and a drop in $FF$. 2) Cell-to-module loss.[55] To date, the most efficient modules have been mainly based on series connections (monolithic interconnected modules). Compared with other structures (e.g., parallel-connected modules), the series connection method does not increase the photocurrent, thus avoiding more $R_s$ loss. However, the resistive loss increased to some extent when the interconnections and busbars were joined. Dai et al. have reported that the rise in cell widths (narrower scribing lines and gaps) would lead to less photocurrent loss (smaller dead area) but a larger resistive loss caused by the TCO compared to a module with the same aperture area,[55a] but a smaller cell width. In addition, the damage and residue caused by the scribing will increase the contact resistance.[9]

**Figure 9** shows that the performance varies with the device area. Both the solar cells and modules are included in the figures. An area of 5 cm$^2$ can be used as the cutoff point; that is, almost all data points belong to the module when the area is >5 cm$^2$. For the module, both the active and aperture areas are used in the figures. The active area is smaller than the aperture area because of the existence of a dead area. The ratio of the active area to the aperture area is called the geometric fill factor (GFF).[55a,56] To date, both active and aperture areas have been reported in the literature. Therefore, we have not strictly distinguished between them in the figures. However, most high-efficiency samples use active areas for calculations. Usually, the reported GFF values are ≈90–96%,[8b,39,56,57] indicating that the efficiency will be subtracted by 1–2% when converting the area from active to aperture. In Figure 9, it is evident that the device area is concentrated in three distinct regions: ≈0.1 cm$^2$, ≈1 cm$^2$, and 10–100 cm$^2$. It is challenging to prepare modules with areas larger than 100 cm$^2$ in the laboratory. Thus, all data points at ≈1000 cm$^2$ belong to devices fabricated by manufacturers. Here, the fabrication methods have not been reported, only efficiency and area are known. Consequently, further discussion is not possible.

Figure 9 clearly shows that the efficiency decreased with increasing area, and the trend is close to a straight line when the $x$-axis is logarithmically plotted. In addition, the extent of performance decline varies with the preparation process. Currently, blade coating is the most successful approach for upscaling, typically achieving efficiencies that surpass those of spin-coated devices within the 10–100 cm$^2$ range, thereby rendering it superior to its competitors. Accompanying the expansion of the device area size, reductions in $J_{SC}$, $V_{OC}$, and $FF$ are observed for the blade-coated devices; however, these decreases are not substantial compared to those of other competitors. In contrast, the spin-coated devices showed a significant reduction in $J_{SC}$ and $FF$, while the vacuum-evaporated devices experienced a noticeable loss in $FF$. Other processes, including slot-die coating, are currently unlikely to rival these three processes (i.e., blade coating, spin-coating, and evaporation) in terms of module performance. The evaporated films are free of pinholes and exhibit homogeneous crystallization, composition, thickness, and morphology,[5a,8a,58] which is crucial for maintaining high $J_{SC}$ and $FF$ values in large-area devices/modules. As illustrated in Figure 9 (also Figure 14, which will be shown later), $J_{SC}$ remained consistently high with increasing area. Unfortunately, the advantages of vacuum evaporation have not yet been realized for $FF$, which exhibits a significant declining trend so far. A more obvious trend can be observed in Figure S2 of the Supporting Information, which contains only

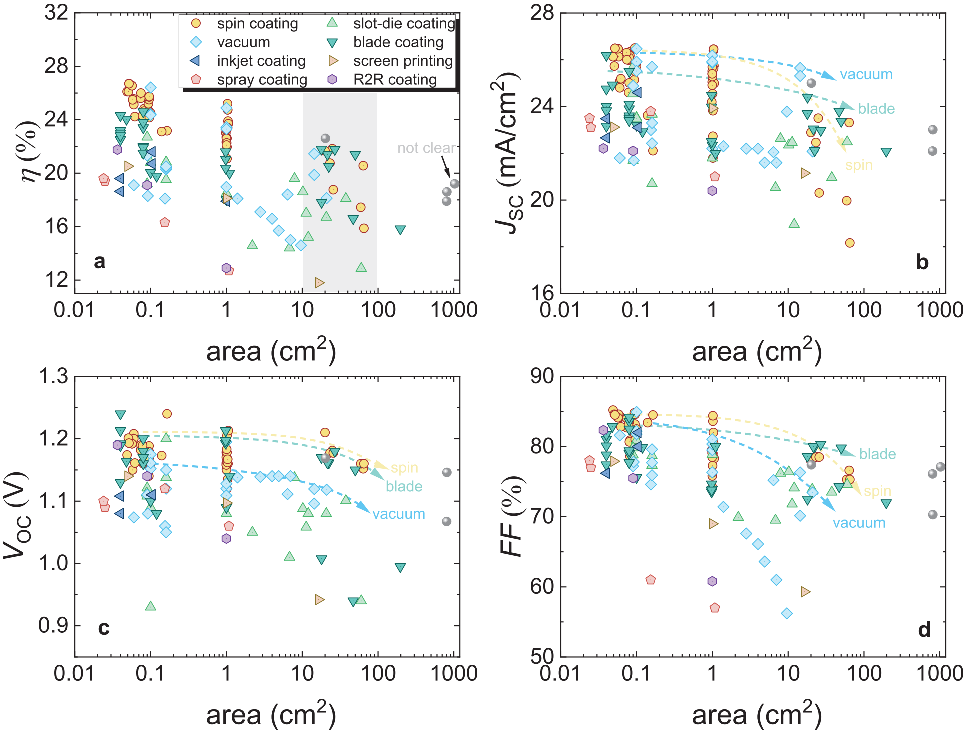

**Figure 9.** Summary of high-efficiency perovskite solar cells and modules with different area sizes. The color of the data points represents the perovskite preparation processes, and the gray spheres indicate that the fabrication process is undisclosed. For all techniques, the device efficiency decreased with increasing area, which is primarily due to the losses in $J_{SC}$ and *FF*.

evaporation data. Currently, we believe that the cause of this issue is the imperfect module fabrication process rather than a problem with the deposition process itself. Furthermore, as the trend of efficiency decreasing with upscaling area approximates a linear relationship when the *x*-axis is plotted logarithmically, indicating that for each tenfold increase in area, the efficiency approximately decreases by a constant value, which is defined as $\eta(A) - \eta(10 \times A)$, where *A* is the device/module area. This metric quantifies the degree of efficiency loss for different technologies during area upscaling. As shown in Figure S8 of the Supporting Information, the data points of spin-coating, vacuum, slot-die coating, and blade coating processes were fitted separately, followed by the calculation of $\eta(A) - \eta(10 \times A)$. The resulting values for the blade coating, vacuum evaporation, spin-coating, and slot-die coating are 1.23%, 1.86%, 2.14%, and 2.60%, respectively. These findings further demonstrate that based on current developments, blade coating and vacuum evaporation processes exhibit the most favorable characteristics in terms of area upscaling.

Apart from lab-scale small (≈0.1 cm$^2$) cells, only ≈1 cm$^2$ cells have been widely investigated. Figure S3 (Supporting Information) and **Figure 10** show a comparison of the performance and fraction of performance within the SQ model, respectively. It can be observed that $\eta/\eta^{SQ}$ decreased by ≈5%, and *FF* and $J_{SC}$ losses dominated the efficiency losses. In particular, the decrease in *FF* is more obvious. We believe that the decrease in $J_{SC}$ may be due to the nonuniformity of the absorber, whereas that of *FF* is thought to be caused by the increase in series resistance. Some top-level devices are managed to avoid efficiency deterioration owing to the low uniformity of the film quality. However, the *FF* loss is more difficult to avoid because the series resistance directly increases with the TCO area. Only one sample with an area of ≈1 cm$^2$ exhibited a high *FF* of ≈86% ($FF/FF^{SQ}$ ≈96%). All the others were below 82%. In Figure S4 of the Supporting Information, we further calculate the nonradiative recombination voltage loss $\Delta V_{OC}^{nonrad}$ and plot it with $E_g^{ip}$ and $J_{SC}/J_{SC}^{SQ}$, separately. It can be seen that either $\Delta V_{OC}^{nonrad}$ or the $J_{SC}/J_{SC}^{SQ}$ ratio of the ≈1 cm$^2$ area devices is comparable to that of the lab-scale devices. Nevertheless, it is difficult to simultaneously maintain these two performances at a high level when scaling up area size. These phenomena point to the problem of reproducibility of the preparation process. Larger areas are more likely to introduce defects and deteriorate the film uniformity. Given that the existing methodologies for mitigating nonradiative recombination voltage loss in laboratory-scale devices have reached a high level of sophistication, it would be valuable to investigate the efficacy of these techniques in the scaling-up process and implement targeted enhancements. We believe that these problems can be partially solved by factories using stable manufacturing technologies. However, further investigations and designs are required to improve *FF*.

**Figure 11** shows the FoMs and potential improvements for the top-level ≈0.1 and ≈1 cm$^2$ devices. The red bar enlarges the most when scaling up the area size, which is mainly caused by the series resistance (see Table 1). Currently, all devices use TCO as one of the electrodes. However, compared to Au and Ag, the TCO films showed lower conductivity. When scaling

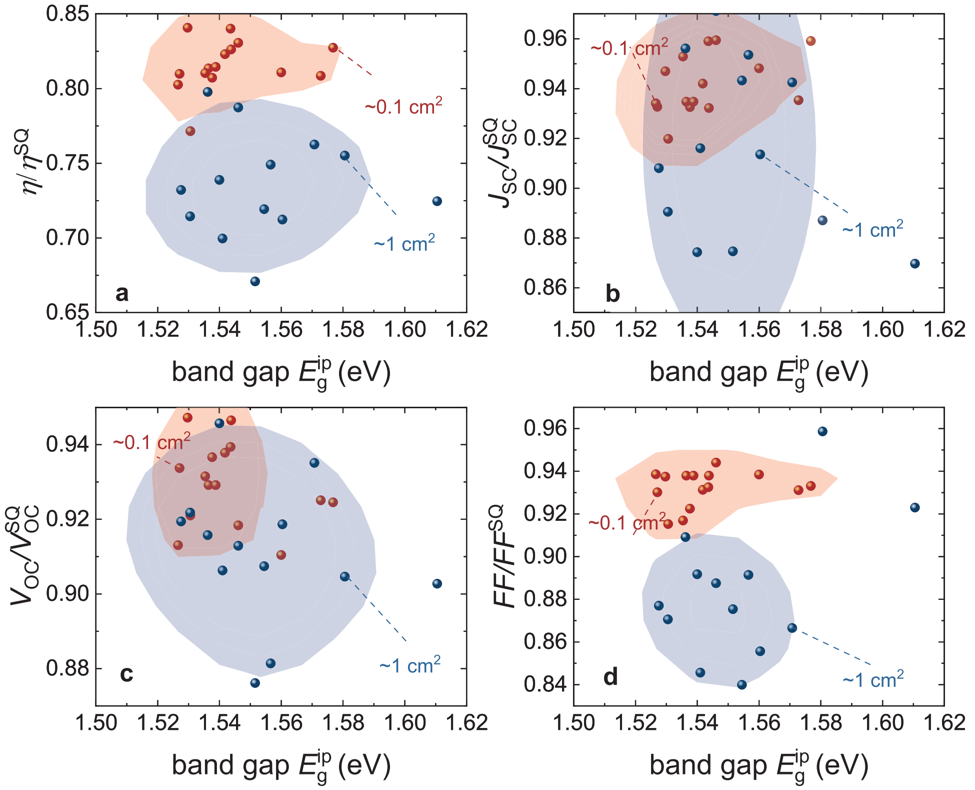

**Figure 10.** Performance as a fraction of the respective value in the SQ model for top-level device with area ≈0.1 cm$^2$ (red) and ≈1 cm$^2$ (blue).

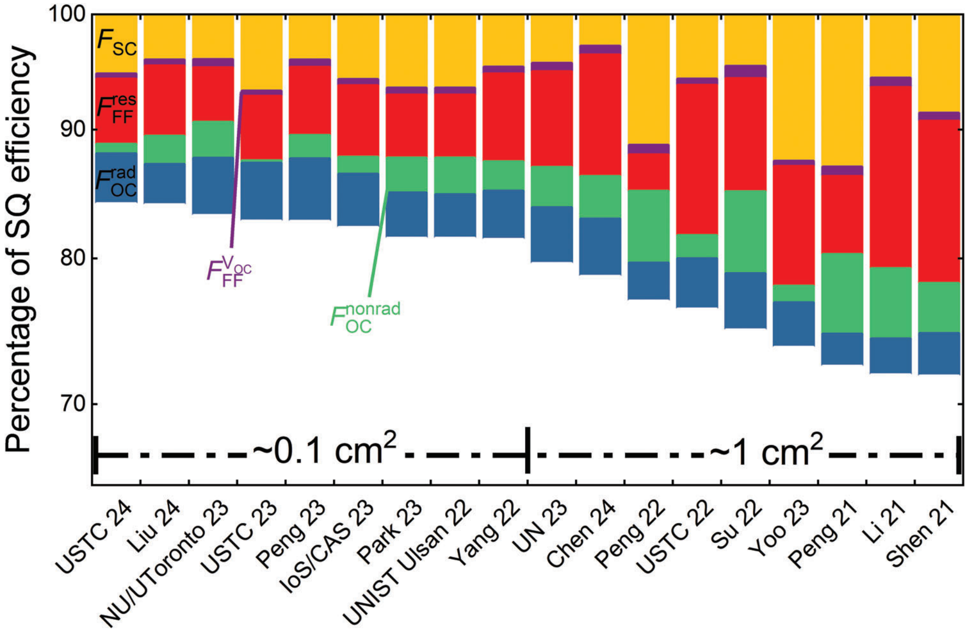

**Figure 11.** Comparison of losses for top-level ≈0.1 cm$^2$ devices and ≈1 cm$^2$ devices. When the device area was upscaled to ≈1 cm$^2$, the *FF* loss due to resistance (red bars) increased the most, mainly because of the finite conductivity of the TCO layers, which caused an inherent compromise between the lateral conductivity (required for good *FF*) and transparency (required for high $J_{sc}$).

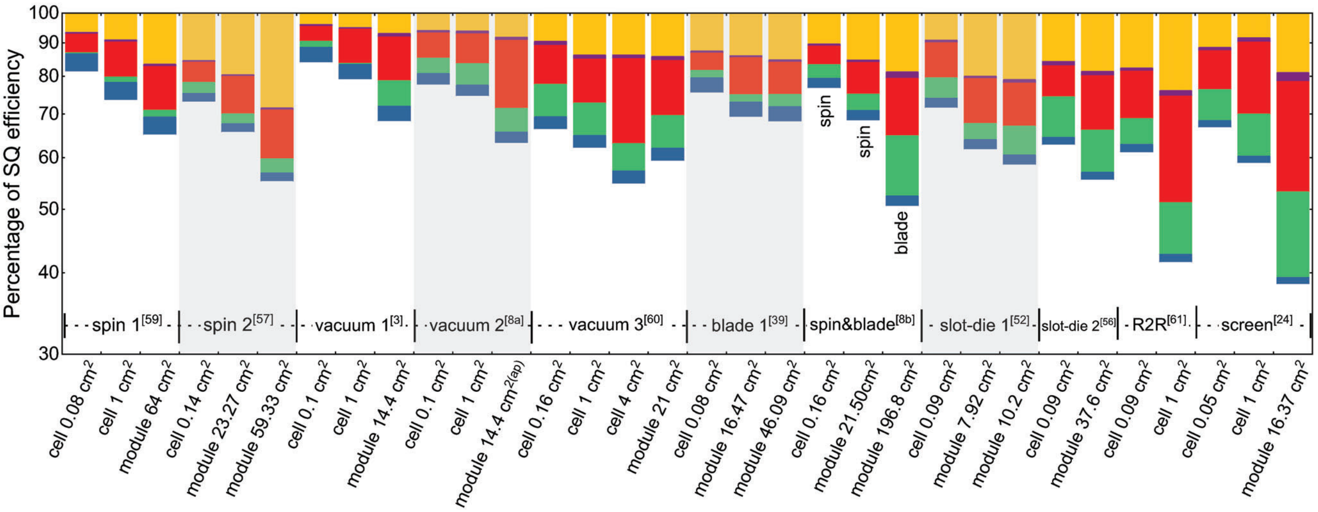

**Figure 12.** Visualized comparison of losses for literature reported differently sized devices/modules with spin-coated,[57,59] vacuum-evaporated,[3,8a,60] blade-coated,[8b,39] slot-die-coated,[52,56] R2R printed (flexible),[61] and screen-printed[24] perovskite. Only the first vacuum module used the aperture area, and all other modules used the active area. For all processes, the $F_{\mathrm{FF}}^{\mathrm{res}}$ (red bar) increases after upscaling from small-area devices to large-area modules. Additionally, the $F_{\mathrm{SC}}$ part (yellow bar), as well as the $F_{\mathrm{OC}}^{\mathrm{nonrad}}$ (green bar) also increased when fabricating the modules.

up the device area, such low conductivity increases the series resistance and thus decreases the *FF*, which further affects the photovoltaic modules. Nevertheless, we find that the samples from Peng et al. showed an obviously larger *FF* than other samples among the ≈1 cm$^2$ devices. In 2021, they presented a regular architecture in which a sparse array of $\mathrm{TiO_2}$ nanorods was used as the electron transport layer, and blending P3HT with CuPc served as the hole transport layer. By introducing ultrathin passivation layers at the perovskite/transport layer interfaces, they demonstrated that the $\mathrm{TiO_2}$ nanorods were incompletely coated with passivation materials, and the nanoscale region of the unpassivated nanorod $\mathrm{TiO_2}$/perovskite interface facilitated localized low-resistance charge transport, which is analogous to the local contact structure used in high-efficiency silicon solar cells. The optimized blended P3HT:CuPc hole transport layer exhibited improved crystallinity and conductivity. Consequently, the fill factor increased from 72.8% to 84.5% for the small-area (≈0.165 cm$^2$) perovskite solar cell. Moreover, the fill factor was still as high as 83.6% for a large-area (≈1.02 cm$^2$) device. One year later, they further optimized the electron transport layer (ETL) and reported an outstanding fill factor of ≈86% (1 cm$^2$). They developed a reverse-doping method to produce high-quality $\mathrm{TiO}_x\mathrm{N}_y$ films by oxidizing sputtered titanium nitride thin films, and used them as electron transport layers. Electrical analysis revealed that the optimum $\mathrm{TiO}_x\mathrm{N}_y$ film exhibited a much higher doping density ($N_\mathrm{D} = 3 \times 10^{17}$ cm$^{-3}$) than that of the $\mathrm{TiO}_x$ film ($N_\mathrm{D} = 5 \times 10^{14}$ cm$^{-3}$). Combined with numerical simulations, they demonstrated that heavy doping of the ETL layer protects against electron depletion that can occur in regions of positive space charge at perovskite/ETL and FTO/ETL heterojunctions. This is a promising deposition method for the commercial fabrication of perovskite devices, as sputtering is already widely used in the photovoltaic industry. From these two reports, it is obvious that developing new transport layers is an important strategy for mitigating *FF* loss.

Unlike solar cells, the areas of reported perovskite modules vary widely. Fortunately, many studies reporting modules have simultaneously presented the performance of solar cells. Representative studies are presented in **Figure 12**. For all the processes, the $F_{\mathrm{FF}}^{\mathrm{res}}$ (the red bar) increases after upscaling from small-area devices to large-area modules. The series resistance of the TCO is one of the reasons discussed above. However, more factors should be considered for the modules. During module preparation, several subcells must be interconnected, which may cause an increase in the series resistance. In addition, scribing the film and laser etching the connection lines (normally called P1, P2, and P3 lines in the community)[57] induce film damage and unremoved residuals, which may decrease the parallel and increase the contact resistance.[9,55a] Additionally, the $F_{\mathrm{SC}}$ part (yellow bar) also increases when fabricating modules, but the changes differ from process to process. The vacuum process showed the smallest increase in $F_{\mathrm{SC}}$, whereas the spin-coating process exhibited the most obvious $F_{\mathrm{SC}}$ increase, suggesting the advantages and disadvantages of these two processes for achieving large-area film uniformity. Nevertheless, the spin-coated cells/modules exhibit the smallest green bar, which indicates a good level of defect control during preparation and upscaling. The module developed by Kim et al. exhibited a high $\eta/\eta^{\mathrm{SQ}}$ of 64.78% on a scale of 64 cm$^2$ (refer to case "spin 1" in the figure).[59] As for the vacuum-evaporated module, Zhou et al. reported a module with a $\eta/\eta^{\mathrm{SQ}}$ of 67.92% on a scale of 14.4 cm$^2$ (refer to case "vacuum 1" in the figure).[3] Among all the cases illustrated in the figure, "blade 1" from Chen et al. showed the smallest decline in all factors during upscaling. The increase in area from 0.08 to 46.09 cm$^2$ resulted in a small decrease in $\eta/\eta^{\mathrm{SQ}}$ from 75.10% to 67.90%.[39] In addition, Bu et al. have got an efficiency of 15.83% on a large module with an effective area of 196.8 cm$^2$ through blade coating (refer to case "spin and blade" in the figure).[8b] To date, these modules represent state-of-the-art modules fabricated in laboratories. Currently, other approaches cannot compete with these

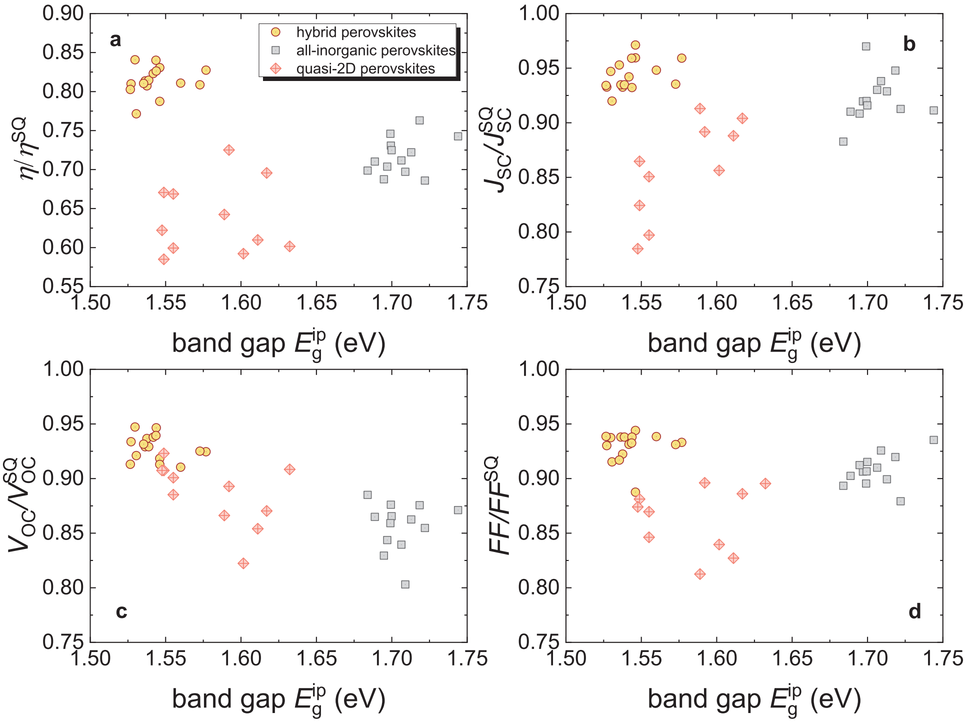

**Figure 13.** Performance as a fraction of the respective value in the SQ model for high-efficiency hybrid perovskite, all-inorganic perovskite, and quasi-2D perovskite. The champion all-inorganic perovskite solar cell had a $\eta/\eta^{SQ}$ of ≈76%, while ≈73% $\eta/\eta^{SQ}$ was observed for the quasi-2D counterpart. They had a similar efficiency of ≈22%.[15c,65] Nevertheless, the limiting factor of all-inorganic perovskite is the ratio $V_{OC}/V_{OC}^{SQ}$, whereas that of quasi-2D perovskite can be attributed to the low $FF/FF^{SQ}$ values.

three methods. Slot-die coating achieved a $\eta/\eta^{SQ}$ of 58.28% on a scale of 10.2 cm$^2$ and 55.23% on a scale of 37.6 cm$^2$.[52,56] Screen printing showed a $\eta/\eta^{SQ}$ of 38.24% on a scale of 16.37 cm$^2$.[24] All of the FoMs exhibited a decrease with increasing area to some extent.

## 5. Stability

Stability is one of the main factors that determines the cost of solar-generated electricity.[62] Typically, the target lifetime of a PV module based on crystalline silicon is 25–30 years. In the absence of mechanical damage due to, e.g., hail, the module can be alive even longer.[63] Achieving better stability can significantly decrease the cost of solar-generated electricity, which cannot be adequately compensated by lowering the price of the modules.[63] Compared with silicon, perovskites are expected to have lower module prices when using printing manufacturing technology. Unfortunately, the traditional perovskites face many stability issues and the high-efficient devices/modules rarely pass the long-term operation standard IEC 61215-1:2016.[19d,64] Changing the material composition and structure makes it possible to improve the device stability. Herein, we focus on analyzing two types of emerging perovskite materials: all-inorganic perovskites and quasi-2D perovskites. Although they have not yet been demonstrated to fully resolve the stability issue, they have furnished some fresh perspectives for the community. All-inorganic perovskites have obvious advantages in terms of thermal stability, and quasi-2D perovskites exhibit better moisture stability than traditional hybrid perovskites. However, as emerging materials, they both exhibit lower efficiencies. On the other hand, it has been demonstrated that reducing the defect density can effectively improve the stability. In the last part of this section, we analyze the loss distribution of cells with the best operational stability, all of which are based on the idea of minimizing the defect density.

The performances of the high-efficiency hybrid perovskites, all-inorganic perovskites, and quasi-2D perovskites are shown in Figure S5 of the Supporting Information. The champion quasi-2D perovskite solar cell shows an efficiency of ≈22%,[15c] while that of the all-inorganic counterpart is slightly lower than 22%.[65,66] As the bandgap of these devices fluctuates from ≈1.5 to ≈1.75 eV, the numerical comparison of performance indicators is meaningless. Therefore, we compared the ratios of the performance parameters relative to their respective values in the SQ model, as shown in **Figure** 13. The champion $\eta/\eta^{SQ}$ of all-inorganic perovskite solar cell was ≈76%, whereas that of the quasi-2D counterpart was slightly lower (≈73%). Additionally, all-inorganic perovskite devices have high values of $J_{SC}/J_{SC}^{SQ}$ (Figure 13b) and $FF/FF^{SQ}$ (Figure 13d), whereas the limiting factor is the $V_{OC}/V_{OC}^{SQ}$ ratio (Figure 13c) and the low $J_{SC}$ value (Figure S5b, Supporting Information) caused by the high bandgap energy. Quasi-2D perovskite solar cells achieved higher $J_{SC}$ values (Figure S5b, Supporting Information). However, $J_{SC}/J_{SC}^{SQ}$ was poor, indicating that the short-circuit current was still a limiting factor. In addition, the $FF/FF^{SQ}$ ratio was not comparable to that of the other two device types. In Figure S6 of the Supporting

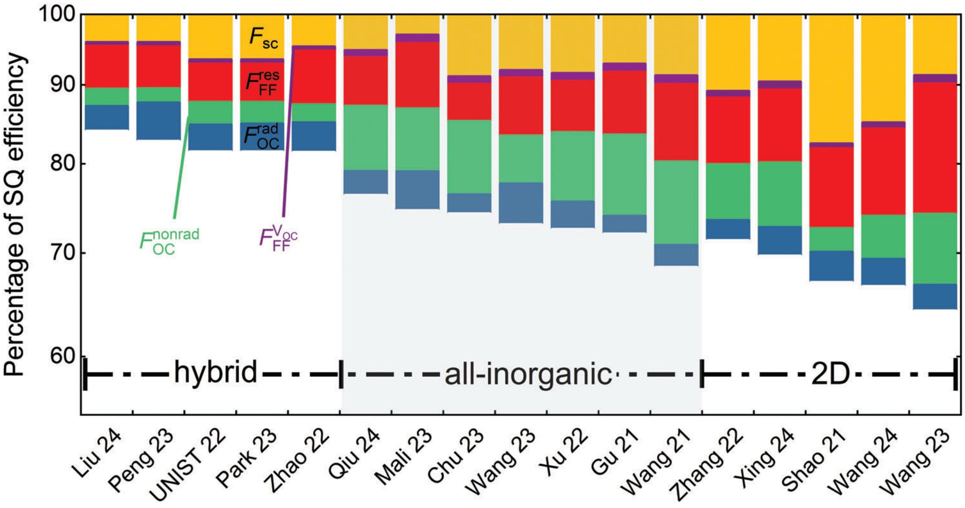

**Figure 14.** Comparison of losses for high-efficiency hybrid perovskites, all-inorganic perovskites, and quasi-2D perovskites. The all-inorganic perovskite devices show large nonradiative recombination voltage loss (green bars) and small photocurrent loss (yellow bars). In contrast, quasi-2D perovskite devices have large photocurrent loss (yellow bars) and small nonradiative recombination voltage loss (green bars).

Information, we additionally calculated the nonradiative $V_{OC}$ loss $\Delta V_{OC}^{nonrad}$ for these devices and plotted it against the bandgap $E_g^{ip}$ and $J_{SC}/J_{SC}^{SQ}$. There are four points in the low $\Delta V_{OC}^{nonrad}$ range, ≈50 mV, for the quasi-2D group, and most of the points fall below 100 mV. However, for the all-inorganic group, the range was 100–250 mV, and only two values were slightly lower than 100 mV.

In brief, the limiting factors for all-inorganic and quasi-2D perovskite solar cells are the nonradiative recombination loss and photocurrent density loss. In **Figure** 14, the loss distribution of some representative cases is presented, which further demonstrates that the $F_{OC}^{nonrad}$ term is the dominant limiting factor for all-inorganic devices, whereas the $F_{SC}$ term dominates the efficiency loss of quasi-2D cells. Our meta-analysis shows that all-inorganic perovskites exhibit similar mobility but have a PL decay time that is more than one order of magnitude shorter.[18c] Strong nonradiative recombination may be responsible for this, which can be attributed to several factors. 1) Defects, including oxygen vacancies, halide vacancies such as iodine vacancies, and undercoordinated $Pb^{2+}$, can act as recombination centers. In most cases, these devices employed a regular structure with $TiO_2$ layers as the electron transport layers, and the perovskite films were prepared on top of them. The interface between $TiO_2$ and perovskite plays a crucial role in interfacial charge transport and perovskite crystallization. However, numerous oxygen vacancies can be easily generated on the $TiO_2$ surface.[65,67] In addition, due to the low formation energy, halide vacancies could form on surfaces and at boundaries,[68] which are often accompanied with a high density of undercoordinated $Pb^{2+}$.[69] 2) Phase transition is another factor. As high-efficiency devices in all-inorganic family are predominantly iodine-based, i.e., $CsPbI_3$, the Goldschmidt tolerance factor for this type of perovskite is typically lower than 0.81,[18c] making phase transitions more likely to occur. $CsPbI_3$ exhibits cubic ($\alpha$), tetragonal ($\beta$), orthorhombic ($\gamma$), and nonperovskite ($\delta$) phases. While the $\alpha$, $\beta$, and $\gamma$ phases can convert into the yellow-phase ($\delta$) at room temperature, this process also induces a significant number of defects.[66,70] 3) The band offset is among the factors that contribute to nonradiative recombination. The transporting layers for $CsPbI_3$ perovskite solar cells are still followed as the hybrid counterparts, with $TiO_2$ and Spiro-OMeTAD being the most commonly used so far.[18c] However, all-inorganic perovskites, such as $CsPbI_3$, have a wide bandgap, leading to a large energy offset that accumulates carriers at the interfaces and thus enhances nonradiative recombination.[69]

The optimization processes employed for hybrid perovskites may not be applicable to all-inorganic perovskites because of the disparities in material properties. In Figure 14, we display the existing high-efficiency all-inorganic devices that utilize effective optimization processes, including interface engineering and additive engineering. For instance, Qiu et al.[65] used 4-aminobutyric acid and 3-amino-1-propanesulfonic acid molecules at the perovskite/$TiO_2$ interface, while Xu et al.[67] used an ionic liquid, 3-sulphonatopropyl acrylate potassium salt for modification. Chu et al.[69] treated the perovskite/air interface with alkali fluorides. Interface engineering has been demonstrated to be effective in passivating defects and optimizing energy band alignment. Wang et al.[66] added 1,2-Di(thiophen-2-yl)ethane-1,2-dione to the precursor solution for the preparation of $\gamma$-$CsPbI_3$, while Mali et al.[71] added guanidinium iodide during vapor deposition of $\gamma$-$CsPbI_3$, and added dimethylammonium iodide (DMAI) to the precursor solution when preparing $\beta$-$CsPbI_3$ using the solution method. The DMAI-assisted growth strategy has been widely used since its inception,[72] as it was employed by Qiu et al.,[65] Chu et al.,[69] and Xu et al. Additive engineering has been shown to enhance phase stability, promote crystallization, and improve morphology, thereby reducing nonradiative recombination loss. Although nonradiative recombination loss still dominates device performance, voltage loss has been reduced to ≈100 mV, compared to ≈160 mV in 2021,[73,74] as indicated by the apparent shortening of the green bar in Figure 14.

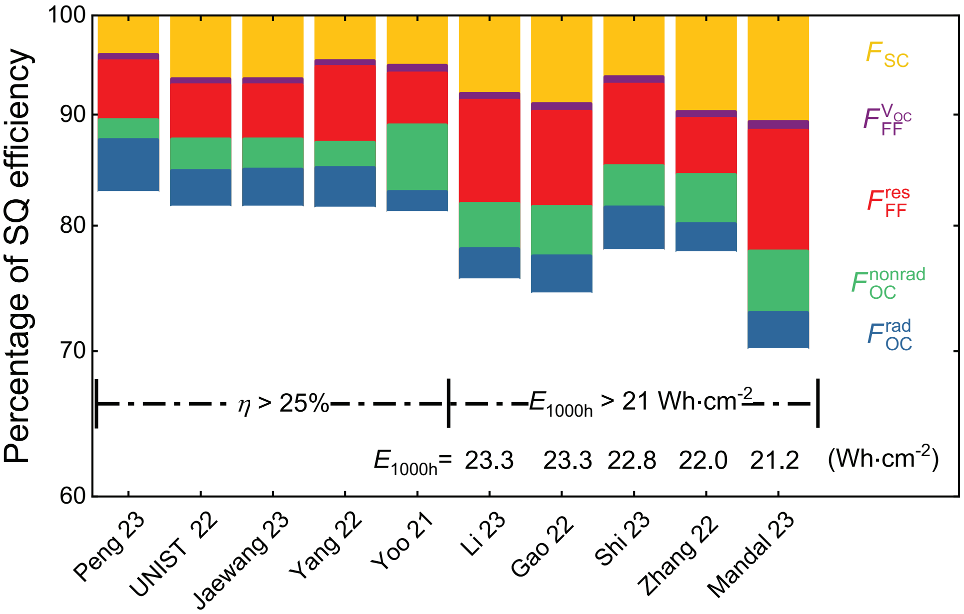

**Figure 15.** Comparison of losses for high-efficient hybrid perovskites and operationally stable perovskite solar cells. Cells with good operational stability show obvious photocurrent and *FF* decrease, which are most likely caused by the increase of series resistance.

Intrinsically, 2D perovskites also have a high bandgap energy ≈2.3 eV, but quasi-2D perovskites can obtain a lower bandgap energy by increasing the n value in the structural formula $A_2B_{n\text{-}1}M_nX_{3n+1}$.[75] At present, highly efficient quasi-2D perovskites have $n \approx 5$, and thus the bandgap has been lowered to ≈1.6 eV.[15c,76] Quasi-2D perovskite devices exhibit low nonradiative voltage losses, but their $J_{SC}/J_{SC}^{SQ}$ is poor. In particular, lower nonradiative voltage losses are always accompanied by more severe $J_{SC}$ losses (Figure S6b, Supporting Information). One possible reason is that quasi-2D perovskites exhibit low vertical conductivity owing to the in-plane crystal preferred orientation and the consequent insulating interlayer bulky cation structure.[76] Shao et al.[76] used 2D Ruddlesden–Popper perovskites as the absorber, which exhibited a preference for growth along the in-plane direction with respect to the substrate, thus resulting in bulky cations of the insulating interlayers hindering out-of-plane charge transfer. Despite the incorporation of FA cations in the film, which extends the absorption range, it only enhances $J_{SC}$ but not $J_{SC}/J_{SC}^{SQ}$. As a result, the $F_{SC}$ loss was quite large, as illustrated in Figure 14. However, the nonradiative recombination voltage losses are remarkably low. Except Shao et al., the high-efficiency devices depicted in Figure 14 are all based on alternating cation perovskite absorbers. Currently, these films are generally thin, for example, ≈390 nm by Zhang and Park;[15c] ≈400 nm by Xing et al.;[77] and ≈430 nm by Wang et al.[78] Apart from that, Wang et al.[79] employed an intermediate phase-assisted sequential deposition strategy, leading to a thickness of ≈670 nm (in contrast, the others in the figure were prepared using a single spin-coating method). Unfortunately, the loss of *FF*-related aspects was too large, reducing the efficiency of the device.

Although emerging perovskites have attracted much attention, the most operationally stable perovskites are still based on hybrid compositions so far.[17] Operational stability test energy yield $E_{1000h}$ is an indicator that can quantitatively evaluate the stability of the cell, as described by Equation (11). **Figure 15** shows the loss distribution of the highly stable devices with $E_{1000h} > 20$ Wh cm$^{-2}$. Compared with the high-efficiency devices ($\eta \geq 25\%$), they show an obvious loss distribution in terms of yellow bars (photocurrent loss) and red bars (*FF* loss). The primary cause of the losses that have emerged is the increase in series resistance. The devices shown in the figure exhibit high operational stability by lowering the trap density.[12c,80] Surface passivation with organic compounds is the most popular method.[12c,80a,c] However, the low conductivity of organic compounds may cause an increase in the series resistance, which ultimately affects $F_{FF}^{res}$ and $F_{SC}$. Li et al.,[12c] Gao et al.,[80a] and Zhang et al.[80c] have all adopted this method. While Shi et al.[80b] employed additive engineering to introduce hydrophobic organic compounds rather than surface passivation.

## 6. Mitigation Strategies

The above analysis shows that the primary losses limiting different process technology routes vary; therefore, different mitigation strategies should be applied. **Table 2** summarizes the challenges and mitigation strategies for each route. The vacuum evaporation process is a promising scalable process which can fabricate devices exhibiting $J_{SC}/J_{SC}^{SQ}$ values as good as spin-coated devices benefiting from the uniform, homogeneous, and pinhole-free films. Moreover, the evaporated devices showed the smallest increase in $J_{SC}$ loss during the cell-to-module process among all methods. Advancements in sequential evaporation technology have enabled a limited number of research groups to fabricate devices with performances comparable to those achieved through spin-coating. However, most evaporated devices still suffer from significant nonradiative recombination and *FF* losses, as well as significant degradation in *FF* during the module fabrication process. In the latter part of this section, we discuss generic

**Table 2.** Challenges and mitigation strategies for perovskite toward commercialization. *Generic mitigation strategies for *FF* loss: 1) enhancing the conductivity of the intrinsic perovskite layer; 2) improving the carrier extraction velocity of the transport layers, which not only increases the fill factor but also releases the limitation on film thickness; and 3) optimizing the film quality, such as increasing the ratio of grain size to film thickness.

| Items | Challenges | Strategies |
|---|---|---|
| Vacuum-evaporation | 1) More diversified effective additive, passivation technologies, and film compositions; 2) production cost; 3) *FF* loss | 1) Utilizing extensive experience in the field of solution process; 2) developing vacuum-compatible interface engineering and transport layer preparation technologies; 3) increasing evaporation rate; 4) generic mitigation strategies for *FF* loss* |
| Blade and slot-die coating | 1) Photocurrent losses or a trade-off relationship between $J_{SC}$ and $V_{OC}$; 2) competing relationship between film quality and film thickness/composition caused by the use of high-boiling solvents; 3) *FF* loss (for slot-die coating) | 1) Improving preparation setup/process to promote solvent evaporation; 2) exploring efficient low-boiling point solvents; 3) utilizing additive engineering and post-treatment to optimize negative factors such as voids, poorly conductive materials, amorphous regions, etc. 4) generic mitigation strategies for *FF* loss* |
| Inkjet printing, screen printing, and spray coating | 1) Competing relationship between solution properties and film quality; 2) nonradiative recombination voltage loss; 3) *FF* loss | 1) More effective additives engineering that can simultaneously improve the solution properties (such as viscosity, surface tension, and contact angle) and perovskite film quality (lower nonradiative recombination); 2) generic mitigation strategies for *FF* loss* |
| Upscaling | 1) *FF* loss; 2) photocurrent loss | 1) TCO design and optimization; 2) scribing/etching processes optimization to solve film damage and residue problem; 3) module design to lower the dead area; 4) enhancing the lateral homogeneities and local compositional homogeneities |
| Quasi-2D perovskite | 1) Photocurrent loss caused by low absorber thickness (< 500 nm) and low vertical conductivity; 2) *FF* loss | 1) Regulation of crystal orientation and film growth; 2) generic mitigation strategies for *FF* loss* |
| All-inorganic perovskite | Nonradiative recombination voltage loss | More effective film growth and defect passivation technology |
| Stable cells with $E_{1000h} > 20$ Wh cm$^{-2}$ | Photocurrent and *FF* loss caused by low conductivity of organic additive and passivation materials | 1) Series resistance optimization; 2) generic mitigation strategies for *FF* loss* |

mitigation strategies for the *FF* loss in detail. Moving forward, we believe that further research should focus on leveraging the experiences in the spin-coating field and exploring diversified additive engineering, passivation technology, and film composition. Furthermore, optimizing the carrier extraction velocity to accelerate the development of thick-absorber-based devices holds great promise for improving the device performance. However, production cost is a crucial factor to consider alongside the improvement in cell and module performance. Abzieher et al. have indicated that only when the number of linear sources is ≥10 and the deposition rate is ≥720 nm min$^{-1}$ can the capital expenditures of vacuum method be comparable to that of solution processing.[6] Currently, however, the deposition rate is only around 10 nm min$^{-1}$.[6] Therefore, it is essential to increase the deposition rate in the next step, which is expected to result in additional performance loss. Moreover, so far, many devices only use vacuum evaporation processes for the preparation of perovskite films and metal electrodes, while the others aspects are mostly solution-based, such as interface passivation technologies and transport layer preparation. This implies that the vacuum process must be interrupted, which is undesirable for large-scale manufacturing. Hence, it is necessary to develop vacuum-compatible interface technologies and transport-layer preparation methods.

Printing processes are typically cost-effective,[4a,b] which is important for commercialization. Based on the loss distribution analysis, we divided printing-related processes into two groups. The first group includes blade coating and slot-die coating. In this group, the devices showed high photocurrent losses or a trade-off relationship between $J_{SC}$ and $V_{OC}$, which may be due to the inadequate solvent volatilization process of the wet films when compared with spin-coating process.[81] A more in-depth reason is the competing relationship between film quality and film thickness/composition caused by the use of high-boiling point solvents. High-boiling-point solvents, such as DMSO, which volatilize slowly during the blade coating and slot-die coating processes, are prone to forming voids inside the film, further inducing the formation of poorly conductive materials and amorphous regions, resulting in film quality deterioration and device performance degradation. To maintain film quality, the film thickness can be reduced to promote solvent volatilization, or by increasing the MA content and decreasing the FA content in the composition. However, the former reduced $J_{SC}/J_{SC}^{SQ}$, and the latter lowered $J_{SC}$. There are several promising method to address the problem. 1) Improving the preparation setup/process to promote solvent volatilization, such as using air-blow (or air knife) equipment, which has been widely adopted, or heating the substrate, which may induce the formation of "polygon domains" and "coffee ring effects" with negative consequences for film growth and performance.[45] 2) Exploring efficient low-boiling point solvents to replace the high-boiling point solvents. 3) Utilizing additive engineering and post-treatment to optimize negative features such as voids, poorly conductive materials, and amorphous regions.

The second group includes inkjet printing, screen printing, and spray coating. The corresponding devices exhibited a large nonradiative recombination loss. Commonly, extra additives are required to adjust solution properties such as viscosity, surface tension, and contact angle when using these preparation methods.[4a,b] It is not reasonable to anticipate that all these additives will have a substantially positive impact on the film quality, resulting in satisfactory performance comparable to that of the spin-coated device. Typically, issues with the film quality lead to significant nonradiative recombination. Therefore, further research on more effective additives that can simultaneously improve solution properties and perovskite film quality is necessary.

During the upscaling process, the largest loss generally originates from *FF*, which can be attributed to the high resistance of the TCO films. TCO glasses are the default substrates for perovskite devices. Moreover, they still appear to be irreplaceable in the preparation of single-junction modules. However, the conductivity of TCOs is never comparable to that of metals such as silver and copper. The influence of the high series resistance increases when the device area is increased. Developing high carrier mobility TCOs can mitigate this problem.[55b] In addition, other types of solar cells/modules can combine Ag grids with TCOs to achieve an optimum balance between transparency and lateral conductivity. However, this type of work has not been reported thus far for halide perovskites using TCO substrates. Therefore, more effort should be invested in TCO design and optimization. In addition, the module fabrication process further reduced the *FF*. To fabricate a module, interconnections are necessary, which increase the series resistance.[5] Meanwhile, inevitable scribing/etching processes, and residues would cause shunting and/or increase the series resistance.[4b,9] Apart from the *FF* loss, photocurrent loss is the second largest cell-to-module loss and is mainly caused by the dead area, which cannot be avoided but can be mitigated with further optimization and better line scribing technique.[55a] Furthermore, lateral inhomogeneities and local compositional inhomogeneities contribute to the cell-to-module efficiency gap.[55b] To date, although many large-area perovskite modules have utilized scalable processes for perovskite film preparation, the majority still employ spin-coating technology for the preparation of transport and passivation layers, which may result in lateral inhomogeneities within the module, leading to performance loss. On the other hand, perovskite films are always demonstrated local compositional heterogeneities owing to ion migration, phase separation, and other factors, resulting in alterations to the local electrical properties of the films. This issue is likely exacerbated during the scale-up process. Enhancing the lateral homogeneities and local compositional homogeneities of a module can potentially improve the performance.

All-inorganic perovskites possess a higher temperature tolerance than hybrid perovskites; however, their performance is limited by defect-induced nonradiative recombination. Therefore, it is imperative to develop targeted passivation technologies to overcome this limitation. In contrast, quasi-2D perovskites intrinsically have low nonradiative recombination losses; however, their efficiency is constrained by the photocurrent and resistive losses. More efforts should be devoted to film growth and crystal orientation modulation. For the most operationally stable hybrid perovskite solar cells ($E_{1000h} > 20$ Wh cm$^{-2}$), the losses in the photocurrent and *FF* are dominant relative to the $V_{OC}$ loss, which can be attributed to the low electrical conductivity of the passivation materials. Thus, the development of new strategies to reduce the series resistance of devices is required to solve this problem.

Finally, we delve into generic mitigation strategies for *FF* losses. Throughout the analysis, *FF* loss was consistently either the first- or second-largest individual loss, highlighting its immense significance. *FF* losses can originate from various sources, necessitating tailored solutions for each cause. Nevertheless, some generic solutions can be considered, such as reducing the series resistance of the absorber layer. For the entire device, the thickness of the perovskite film significantly exceeds that of the other layers (except for the TCO electrode); however, as an intrinsic material, the conductivity of the perovskite film is limited. Another generic option to improve the *FF* is to enhance the carrier extraction velocity of the transport layers. This not only improves the *FF*, but also indirectly determines the short-circuit current density, as the effective carrier extraction velocity limits the film thickness and, hence, the short-circuit current density. According to theoretical research conducted by Akel et al., a sufficiently long diffusion length of an absorber (commonly expressed as "$L_D \gg d$") is a necessary but not a sufficient condition for efficient charge collection. A more crucial determinant of efficient charge collection is "$S_{ext}\tau_{bulk} \gg d$", where $\tau_{bulk}$ is the lifetime of the absorber, and $S_{ext}$ is the extraction velocity in the transport layer, which refers to the rate at which electrons (or holes) are transported through the transport layers. Meanwhile, $S_{ext}$ is proportional to the mobility of the transport layer and the potential difference across the transport layer. Therefore, the properties of the transport layer have a direct impact on the fill factor and short-circuit current.[38] Experimental findings by Wang et al. further corroborate the relationship between $S_{ext}$ and *FF*, which is especially vital for thick-film devices. They emphasized that not only the mobility-lifetime product of the absorber and the interface recombination velocity, but also the properties of the transport layer (e.g., mobility) are critical factors in charge-carrier extraction. To achieve the same charge-carrier collection efficiency for thicker absorber layers, the mobility in the transport layer must increase proportionally with the thickness increase.[82] In the preceding discussion, it has been noted that Peng et al. successfully fabricated ≈1 cm$^2$ devices with a fill factor up to 86%, utilizing well-designed transport layers, such as a sparse array of $TiO_2$ nanorods[83] and a heavy doping $TiO_xN_y$ film.[84] Other examples abound, for instance, Zhou et al. developed a multifunctional organic hole transport layer "T2" based on a thiomethyl-substituted fluorene arm, resulting in an *FF* increased from 82% to 85% compared to the typical Spiro-OMeTAD hole transport layer.[3] Yu et al. improved the FF from 77% to 84% through the design of $NiO_x$/SAMs double hole transport layer.[85] Moreover, there is a third alternative for increasing the *FF* by enhancing the quality of the perovskite film. According to the criterion from Akel et al., both $\tau_{bulk}$ and $S_{ext}$ are crucial for effective charge collection.[38] Enhancing the quality of the film and minimizing the impact of recombination centers can improve $\tau_{bulk}$. Chiang et al. attained a high fill factor of 86% for $MAPbI_3$ solar cells by optimizing grain size to reach a size of 1.5 µm, while the film thickness was ≈470 nm for comparison.[86] However, given that the nonradiative recombination loss in films is presently minimal, it is likely to be challenging to further increase the *FF* through this approach.

## 7. Conclusion and Outlooks

In this study, we quantified the development of efficiency-limiting loss mechanisms for halide perovskite solar cells on the technological path from small-area cells to large-area modules. To enable comparability of the quantities of interest within the wider material family of halide perovskites, we calculated the performance fractions in the SQ model, nonradiative recombination loss, and five figures of merit to visualize the photocurrent losses, resistive losses, and recombination losses. All these data were used to analyze changes in the loss distribution during the adoption of commercial preparation techniques, upscaling area sizes, and enhancement of stability.

To date, perovskite solar cells have achieved an efficiency of over 26%[1] and have approached 85% of the SQ limit. However, for a module with an area >800 cm$^2$, the efficiency and $\eta/\eta^{SQ}$ are only ≈19%[2] and ≈60%, respectively. The widely used spin-coating process is not suitable for large-area photovoltaics and exhibits significant photocurrent degradation upon upscaling. Vacuum-evaporated devices have made the most significant advancements in recent years, with the recorded efficiency increasing from 20.5%[20] (in 2022) to 26.21%[3] (in 2024). These devices can achieve high current densities and exhibit minimal photocurrent degradation during upscaling. However, the potential for thicker film preparation has not yet been fully realized owing to the limitation in the carrier extraction velocity. Meanwhile, *FF* degradation was too pronounced when upscaling the device/module area. In addition, it is necessary to explore approaches to increase the evaporation rate and to use a vacuum process for the entire device preparation procedure in the future, which will directly impact the commercialization prospects. Currently, blade coating is considered the most effective method for scaling up, as it typically exhibits the highest module efficiencies within the 10–100 cm$^2$ area range and experiences the least degradation of performance during the upscaling process. Slot-die coating is another promising technology for commercialization; however, at present, the performance of both lab-sized cells and large-area modules is inferior to that of evaporated and blade-coated cells/modules. However, in light of its similar preparation principle and technical issues associated with blade coating, it is expected that slot-die coating will also undergo rapid progress in the future. The primary challenge with blade coating and slot-die coating is the competing relationship between film quality and thickness/composition owing to the use of high-boiling-point solvents. Although other processes, such as inkjet printing, screen printing, and spray coating, have made good progress, they are currently unable to compete with vacuum evaporation, blade coating, and slot-die coating in the field of module fabrication when compared side-by-side. In this study, we discuss potential mitigation strategies to address these challenges.

In the past decade, perovskite solar cells have undergone rapid development. The focus of performance optimization has mainly been on reducing energy loss and increasing open-circuit voltage. However, with the development of defect passivation techniques, nonradiative recombination voltage loss no longer dominates the device performance, which can be reduced to less than 50 mV in lab-scale spin-coated, evaporated, and blade-coated devices. Consequently, the *FF* loss overtakes the nonradiative recombination voltage loss as the dominant performance factor. This is also evident in a side-by-side comparison with c-Si and GaAs devices (Figure 1), where the perovskite cell/module shows a much larger *FF* loss. Additionally, solar cells prepared using scalable methods (such as vacuum evaporation, slot-die coating, inkjet printing, screen printing, and spray printing methods), as well as emerging perovskite cells (such as quasi-2D perovskite), suffer from large *FF* losses. Furthermore, the process of increasing the device size and improving the stability is always accompanied by an increase in the *FF* loss. The sources of *FF* loss are diverse and require various mitigation strategies. In this study, we discuss these strategies in detail. Here, we would like to emphasize one of the generic strategies: improving the carrier extraction velocity of the transport layer. It has been proven that efficient charge collection requires the condition "$S_{ext}\tau_{bulk} \gg d$"[38] to be satisfied. Given the difficulty in further increasing $\tau_{bulk}$, the carrier exchange rate $S_{ext}$, which depends on the properties of the transport layers, is crucial. An increased $S_{ext}$ value not only improves the *FF* but also relaxes the limitation on the film thickness $d$, thereby enabling an increase in film thickness and a further enhancement of the short-circuit current density. It is important to note that in many cases, the short-circuit current density accounts for two of the largest loss distributions along with the *FF*.

## 8. Performances Tables

Here, we list the details of the data points discussed in this study. For the modules, equivalent $V_{OC}$ and $J_{SC}$ for each individual subcell are calculated by dividing (multiplying) reported $V_{OC}$ ($J_{SC}$) value to connected subcell numbers.

**Table 3.** Performance of the single-junction cell with certified efficiency, corresponding to Figure 1a.

| Classification | $E_g^{ip}$ [eV] | $V_{OC}$ [V] | $J_{SC}$ [mA cm$^{-2}$] | *FF* [%] | $\eta$ [%] | Area [cm$^2$] | Refs. |
|---|---|---|---|---|---|---|---|
| GaAs | 1.42 | 1.127 | 29.78 | 86.7 | 29.1 | 0.998 $^{ap}$ | [88] |
| c-Si | 1.09 | 0.7434 | 42.6 | 86.2 | 27.3 | 243.1 $^{da}$ | [1b] |
| Perovskite | 1.53 | 1.193 | 26.49 | 84.5 | 26.7 | 0.0519 $^{da}$ | [1b] |
| CIGS | 1.09 | 0.734 | 39.58 | 80.4 | 23.35 | 1.043 $^{da}$ | [89] |
| CdTe | 1.40 | 0.8996 | 31.40 | 79.3 | 22.4 | 0.4497 $^{da}$ | [90] |
| OPV | 1.45 | 0.891 | 26.69 | 80.84 | 19.23 | 0.03084 $^{ac}$ | [91] |

**Table 4.** Performance of single-junction modules with certified efficiency corresponding to Figure 1b. The subcell numbers are listed in table. We estimated the cell numbers (labeled with $^{es}$) according to the reported $V_{OC}$ value for parts of the modules that had not stated the cell number.

| Classification | $E_g^{ip}$ [eV] | $V_{OC}$ [V] | $J_{SC}$ [mA cm$^{-2}$] | *FF* [%] | $\eta$ [%] | Area [cm$^2$] | Refs. |
|---|---|---|---|---|---|---|---|
| GaAs (10 cells $^{es}$) | 1.42 | 1.108 | 26.58 | 85.3 | 25.1 | 866.45 $^{ap}$ | [92] |
| c-Si (112 cells) | 1.14 | 0.742 | 40.54 | 82.8 | 24.9 | 17 753 $^{da}$ | [1b] |
| CdTe (260 cells $^{es}$) | 1.42 | 0.876 | 28.91 | 76.8 | 19.5 | 23 582 $^{da}$ | [19b] |
| CIGS (70 cells) | 1.12 | 0.686 | 37.95 | 73.7 | 19.2 | 841$^{ap}$ | [93] |
| Perovskite (39 cells) | 1.57 | 1.146 | 23.01 | 70.3 | 18.6 | 809.9 $^{da}$ | [94] |
| OPV (38 cells $^{es}$) | 1.41 | 0.832 | 23.32 | 74.6 | 14.5 | 204.11 $^{da}$ | [2] |

**Table 5.** Performances, areas, and perovskite preparation processes for high-efficiency hybrid perovskite solar cells and modules. The active area is defined as the default device area for the cells. For modules, label $^{M}$ is noted on the upper right of the area, and the designated, active, and aperture areas are labeled as $^{\mathrm{da}}$, $^{\mathrm{ac}}$, and $^{\mathrm{ap}}$, respectively.

| $E_g^{\mathrm{ip}}$ [eV] | $V_{OC}$ [V] | $J_{SC}$ [mA cm$^{-2}$] | $FF$ [%] | $\eta$ [%] | Area [cm$^2$] | Preparation | Refs. |
|---|---|---|---|---|---|---|---|
| 1.54 | 1.192 | 26.47 | 84.11 | 26.54 | 0.057 | Spin | [95] |
| 1.55 | 1.174 | 26.13 | 85.2 | 26.15 | 0.05 | Spin | [1c] |
| 1.55 | 1.167 | 26.45 | 80.1 | 24.74 | 1.04 | Spin | [1c] |
| 1.54 | 1.201 | 25.73 | 84.6 | 26.1 | $0.051^{\mathrm{da}}$ | Spin | [90] |
| 1.54 | 1.19 | 26 | 84 | 26 | $0.0746^{\mathrm{da}}$ | Spin | [94] |
| 1.56 | 1.181 | 25.14 | 84.8 | 25.2 | 0.0937 | Spin | [19a] |
| 1.54 | 1.1885 | 25.74 | 83.2 | 25.5 | 0.0954 | Spin | [96] |
| 1.54 | 1.179 | 25.8 | 84.6 | 25.7 | 0.09597 | Spin | [19b] |
| 1.58 | 1.208 | 25.08 | 84.37 | 25.56 | 0.06 | Spin | [34] |
| 1.58 | 1.2 | 24.8 | 84.14 | 25.13 | 0.06 | Spin | [34] |
| 1.53 | 1.16 | 25.73 | 82.5 | 24.5 | 0.1 | Spin | [12c] |
| 1.53 | 1.176 | 26.09 | 83.84 | 25.72 | 0.0803 | Spin | [59] |
| 1.53 | 1.158 | 25.4 | 79.05 | 23.25 | 1 | Spin | [59] |
| 1.53 | 12.1 | 2.289 | 77.9 | 21.67 | $20^{M\ \mathrm{ac}}$ | Spin | [59] |
| 1.53 | 18.43 | 1.457 | 76.6 | 20.56 | $64^{M\ \mathrm{ac}}$ | Spin | [59] |
| 1.54 | 1.179 | 25.8 | 84.6 | 25.73 | 0.09597 | Spin | [19g] |
| 1.53 | 1.15 | 26.13 | 84.6 | 25.49 | 0.058 | Spin | [29] |
| 1.54 | 1.182 | 26.3 | 82.7 | 25.6 | 0.0741 | Spin | [33] |
| 1.54 | 1.162 | 26.39 | 82 | 25.2 | $1.0347^{\mathrm{da}}$ | Spin | [90] |
| 1.55 | 1.12 | 23.82 | 79 | 21.08 | 1.02 | Spin | [97] |
| 1.61 | 1.205 | 21.8 | 83.6 | 21.96 | 1.02 | Spin | [83] |
| 1.58 | 1.178 | 22.73 | 84.4 | 22.6 | 1.0189 | Spin | [98] |
| 1.57 | 1.213 | 24.99 | 78.3 | 23.7 | 1.062 | Spin | [19b] |
| 1.56 | 1.135 | 25.625 | 80.5 | 23.41 | 1.04 | Spin | [99] |
| 1.53 | 1.161 | 24.91 | 78.47 | 22.69 | 1 | Spin | [100] |
| 1.55 | 1.16 | 25.69 | 75.8 | 22.6 | 1.00142 | Spin | [101] |
| 1.56 | 1.183 | 24.55 | 77.27 | 22.26 | 1.0085 | Spin | [102] |
| 1.54 | 1.15 | 25.283 | 76.27 | 22.1 | 1.0036 | Spin | [103] |
| 1.53 | 1.158 | 25.4 | 79.05 | 23.25 | 1 | Spin | [59] |
| 1.58 | 1.17 | 25.05 | 79.48 | 23.3 | 1 | Spin | [34] |
| 1.53 | 1.173 | 23.62 | 83.4 | 23.11 | 0.14 | Spin | [57] |
| 1.53 | 1.17725 | 22.45917 | 78.5 | 20.75 | $23.27^{M\ \mathrm{ac}}$ | Spin | [57] |
| 1.53 | 1.17725 | 20.304 | 78.5 | 18.76 | $25.74^{M\ \mathrm{ap}}$ | Spin | [57] |
| 1.53 | 1.16 | 19.9716 | 75.3 | 17.44 | $59.33^{M\ \mathrm{ac}}$ | Spin | [57] |
| 1.53 | 1.16 | 18.168 | 75.3 | 15.87 | $65.22^{M\ \mathrm{ap}}$ | Spin | [57] |
| 1.54 | 1.175 | 26.47 | 84.94 | 26.41 | $0.1^{\mathrm{ap}}$ | vacuum | [3] |
| 1.54 | 1.195 | 26.18 | 79.5 | 24.88 | $1^{\mathrm{ap}}$ | vacuum | [3] |
| 1.54 | 1.096 | 25.65 | 76.31 | 21.45 | $14.4^{M}$ | vacuum | [3] |
| 1.52 | 1.11 | 24.88 | 77.2 | 21.32 | 0.09 | Vacuum | [30] |
| 1.52 | 1.092 | 23.78 | 56.22 | 14.6 | $9.6^{M}$ | Vacuum | [30] |
| 1.61 | 1.06 | 23 | 74.6 | 18.1 | 0.155 | Vacuum | [35] |
| 1.59 | 1.12 | 23.3 | 77.7 | 20.28 | 0.16 | Vacuum | [60] |
| 1.59 | 1.12 | 22.2 | 76.32 | 18.97 | 1 | Vacuum | [60] |
| 1.59 | 6.71 | 3.68 | 73.44 | 18.13 | $21^{M\ \mathrm{ac}}$ | Vacuum | [60] |
| 1.54 | 1.152 | 25.92 | 81.78 | 24.42 | 0.1 | Vacuum | [8a] |
| 1.54 | 1.128 | 25.87 | 80.36 | 23.44 | 1 | Vacuum | [8a] |
| 1.54 | 1.1195 | 25.308 | 70.14 | 19.87 | $14.4^{M\ \mathrm{ap}}$ | Vacuum | [8a] |
| 1.53 | 1.05 | 25.7 | 75.91 | 20.4 | 0.16 | Vacuum | [104] |

(*Continued*)

**Table 5.** (Continued)

| $E_g^{ip}$ [eV] | $V_{OC}$ [V] | $J_{SC}$ [mA cm$^{-2}$] | *FF* [%] | $\eta$ [%] | Area [cm$^2$] | Preparation | Refs. |
|---|---|---|---|---|---|---|---|
| 1.55 | 1.161 | 25.52 | 82.2 | 24.36 | 0.1 | Vacuum | [31] |
| 1.59 | 1.138 | 22.3 | 71.4 | 18.1 | 1.4 | Vacuum | [36] |
| 1.59 | 1.11129 | 22.05 | 75.2 | 18.4 | $6.4^{M\ \mathrm{ac}}$ | Vacuum | [36] |
| 1.55 | 1.17 | 25.5 | 82.5 | 24.6 | $0.08^{\mathrm{ac}}$ | Blade | [8c] |
| 1.55 | 1.18 | 22.98 | 80.32 | 21.78 | $26.9^{M\ \mathrm{ap}}$ | Blade | [8c] |
| 1.54 | 1.13 | 26.19 | 81.7 | 24.31 | $0.04^{\mathrm{ac}}$ | Blade | [8d] |
| 1.57 | 1.164 | 24.92 | 82.87 | 24.04 | 0.048 | Blade | [105] |
| 1.60 | 1.1 | 23.2 | 75.58 | 20.05 | 0.1 | Blade | [106] |
| 1.60 | 1.09 | 22.35 | 73.93 | 18.02 | 1 | Blade | [106] |
| 1.56 | 1.18 | 23.6 | 79 | 22 | 0.08 | Blade | [41b] |
| 1.56 | 1.2 | 23.5 | 77.7 | 21.9 | 0.08 | Blade | [107] |
| 1.55 | 1.16 | 23.4 | 79.4 | 21.5 | 0.08 | Blade | [41c] |
| 1.61 | 1.14 | 22 | 80 | 20 | 1.1 | Blade | [41c] |
| 1.54 | 1.192 | 24.01 | 81.04 | 23.19 | 0.04 | Blade | [42] |
| 1.54 | 1.193 | 23.98 | 73.54 | 21.04 | 0.98 | Blade | [42] |
| 1.60 | 1.213 | 23.16 | 80.09 | 22.51 | 0.04 | Blade | [42] |
| 1.60 | 1.213 | 22.5 | 74.66 | 20.37 | 0.98 | Blade | [42] |
| 1.54 | 1.17 | 23.9 | 83.6 | 23.4 | 0.08 | Blade | [43] |
| 1.54 | 1.17 | N/A | 77.3 | 18.5 | $35.8^{M\ \mathrm{ap}}$ | Blade | [43] |
| 1.54 | 1.17 | 24.1 | 84.2 | 23.8 | 0.08 | Blade | [39] |
| 1.54 | 1.17 | 21.8 | 78.6 | 20.1 | $17.9^{M\ \mathrm{ap}}$ | Blade | [39] |
| 1.54 | 1.17 | 23.7 | 78.6 | 21.8 | $16.46^{M\ \mathrm{ac}}$ | Blade | [39] |
| 1.54 | 1.15 | 21.5 | 79.8 | 19.7 | $50.1^{M\ \mathrm{ap}}$ | Blade | [39] |
| 1.54 | 1.15 | 23.37 | 79.8 | 21.4 | $46.09^{M\ \mathrm{ac}}$ | Blade | [39] |
| 1.54 | 1.189 | 24.75 | 78.8 | 23 | 0.04 | Blade | [41a] |
| 1.54 | 1.197 | 24.48 | 73.8 | 21.6 | 0.98 | Blade | [41a] |
| 1.61 | 1.24 | 23.82 | 77.4 | 22.8 | 0.04 | Blade | [41a] |
| 1.55 | 1.173 | 24.38 | 83.9 | 24.02 | 0.16 | Spin | [8b] |
| 1.55 | 1.16143 | 23.04167 | 80 | 21.4 | $21.504^{M\ \mathrm{ac}}$ | Spin | [8b] |
| 1.55 | 0.995 | 22.09375 | 72 | 15.83 | $196.8^{M\ \mathrm{ac}}$ | Blade | [8b] |
| 1.55 | 1.16143 | 22.12 | 80 | 20.5 | $22.4^{M\ \mathrm{ap}}$ | Blade | [8b] |
| 1.55 | 0.995 | 21.21 | 72 | 15.3 | $205^{M\ \mathrm{ap}}$ | Blade | [8b] |
| N/A | 1.08 | 22.92 | 79.9 | 19.78 | 0.12 | Blade | [108] |
| N/A | 1.0075 | 24.4 | 72.5 | 17.82 | $18^{M\ \mathrm{ac}}$ | Blade | [108] |
| N/A | 0.94 | 23.8 | 74.3 | 16.6 | $47^{M\ \mathrm{ac}}$ | Blade | [108] |
| 1.52 | 1.121 | 25.7 | 78.8 | 22.7 | 0.09 | Slot-die | [52] |
| 1.52 | 1.1375 | 22.62626 | 76.2 | 19.6 | $7.92^{M\ \mathrm{ac}}$ | Slot-die | [52] |
| 1.5155 | 1.088 | 22.35294 | 76.4 | 18.6 | $10.2^{M\ \mathrm{ac}}$ | Slot-die | [52] |
| 1.59 | 1.09 | 23.53 | 80.9 | 20.8 | 0.1 | Slot-die | [50] |
| 1.59 | 1.01 | 20.53 | 69.5 | 14.4 | $6.8^{M\ \mathrm{ac}}$ | Slot-die | [50] |
| 1.59 | 1.138 | 23.673 | 77.322 | 20.831 | 0.16 | Slot-die | [54] |
| 1.59 | 1.08 | 21.8 | 78.9 | 18.5 | 1 | Slot-die | [109] |
| 1.59 | 1.08 | N/A | 73.9 | 16.7 | $20.77^{M\ \mathrm{ac}}$ | Slot-die | [109] |
| 1.57 | 1.113 | 24.54 | 78.26 | 21.38 | 0.089 | Slot-die | [53] |
| 1.66 | 1.2 | 20.7 | 78.7 | 19.52 | 0.16 | Slot-die | [110] |
| 1.58 | 1.138 | 23.673 | 77.322 | 20.831 | 0.16 | Slot-die | [54] |
| 1.54 | 1.16 | 24.8 | 81.4 | 23.4 | N/A | Slot-die | [21] |
| 1.59 | 1.108 | 21.7 | 79.8 | 19.2 | 0.09 | Slot-die | [56] |
| 1.59 | 1.05833 | 22.46809 | 71.8 | 17 | $11.28^{M\ \mathrm{ac}}$ | Slot-die | [56] |
| 1.59 | 1.10063 | 20.96 | 73.5 | 18.1 | $37.6^{M\ \mathrm{ac}}$ | Slot-die | [56] |

*(Continued)*

**Table 5.** (Continued)

| $E_g^{ip}$ [eV] | $V_{OC}$ [V] | $J_{SC}$ [mA cm$^{-2}$] | *FF* [%] | *η* [%] | Area [cm$^2$] | Preparation | Refs. |
|---|---|---|---|---|---|---|---|
| 1.57 | 1.093 | 22.5 | 77.1 | 19 | N/A | Slot-die | [111] |
| 1.57 | 1.08 | 18.96 | 74.1 | 15.2 | 12 $^{M\ \mathrm{ap}}$ | Slot-die | [111] |
| N/A | 0.94 | 22.49 | 74.6 | 12.87 | 60.08 $^{M\ \mathrm{ac}}$ | Slot-die | [112] |
| 1.14 | 22.1 | 75.5 | 19.1 | 1.14 | N/A | R2R (gravure printing) flexible | [61] |
| 1.19 | 22.21 | 82.33 | 21.76 | 1.19 | 0.0365 | R2R (blade coating) flexible | [22] |
| N/A | 1.11 | 24.6 | 80 | 21.6 | 0.105 | Inkjet | [23] |
| 1.72 | 1.15 | 20.5 | 80.5 | 19 | N/A | Inkjet | [113] |
| 1.60 | 1.108 | 23.48 | 76.2 | 19.6 | 0.004 | Inkjet | [114] |
| 1.60 | N/A | N/A | N/A | 17.9 | 1.01 | Inkjet | [114] |
| 1.61 | 1.11 | 23.1 | 82 | 20.7 | 0.105 | Inkjet | [115] |
| 1.58 | 1.14 | 23.12 | 77.9 | 20.52 | 0.05 | Screen | [24] |
| 1.58 | 1.097 | 23.93 | 69 | 18.12 | 1 | Screen | [24] |
| 1.58 | 0.942 | 21.15 | 59.3 | 11.8 | 16.37 $^{M\ \mathrm{ac}}$ | Screen | [24] |
| N/A | 1.07 | 24.1 | 70.5 | 18.2 | N/A | Spray | [116] |
| 1.61 | 1.09 | 23 | 77.3 | 19.4 | 0.025 | Spray | [117] |
| 1.57 | 1.14 | 22 | 77.8 | 19.5 | N/A | Spray | [118] |
| N/A | 1.1 | 23.5 | 78 | 19.6 | 0.024 | Spray | [25] |
| 1.55 | 1.067 | 22.10 | 76.1 | 17.9 | 800 $^{M\ \mathrm{da}}$ | N/A | [119] |
| N/A | N/A | N/A | 76.9 | 20.5 | 63.98 $^{M}$ | N/A | [120] |
| N/A | 0.83636 | 21.34 | 51 | 9 | 220 $^{M\ \mathrm{ac}}$ | Drop casting | [121] |
| 1.56 | 1.21 | 24.8 | 84.7 | 25.4 | 0.08 | Spin | [122] |
| 1.52 | 1.184 | 25.27 | 83.37 | 24.9 | 0.1 | Spin flexible | [28b] |
| 1.54 | 1.152 | 25.47 | 83.31 | 24.48 | 0.0581 | Spin flexible | [123] |
| 1.54 | 1.136 | 25.36 | 83.57 | 24.08 | N/A | Spin flexible | [124] |
| 1.55 | 1.186 | 25.39 | 83.14 | 25.05 | 0.04 | Spin flexible | [28a] |

**Table 6.** Performances, areas, and perovskite preparation processes for high-efficiency quasi-2D perovskite solar cells.

| $E_g^{ip}$ [eV] | $V_{OC}$ [V] | $J_{SC}$ [mA cm$^{-2}$] | *FF* [%] | *η* [%] | Area [cm$^2$] | Preparation | Refs. |
|---|---|---|---|---|---|---|---|
| 1.55 | 1.18 | 22.45 | 79.53 | 21.07 | 0.02985 | Spin | [76] |
| 1.55 | 1.16 | 23.55 | 67 | 18.38 | 1 | Spin | [76] |
| 1.59 | 1.14 | 23.54 | 73.51 | 19.72 | N/A | Spin (hot-cast) | [79] |
| 1.60 | 1.09 | 21.77 | 76 | 18.06 | 0.05025 | Spin | [125] |
| 1.61 | 1.14 | 22.26 | 74.92 | 18.48 | 0.09 | Spin | [126] |
| 1.63 | 1.23 | 18.22 | 81.2 | 18.2 | 0.03 | Spin (hot-cast) | [127] |
| 1.62 | 1.22 | 19.91 | 78.56 | 19.08 | 0.04 | Spin | [128] |
| 1.55 | 1.16 | 21.37 | 78.88 | 19.55 | 0.08875 | Spin | [129] |
| 1.59 | 1.175 | 22.99 | 81.07 | 22.26 | 0.125 | Spin | [15c] |
| 1.62 | 1.17 | 22.4 | 80.3 | 21 | 0.09 | Blade | [77] |
| 1.56 | 1.16 | 22.86 | 78.53 | 20.9 | N/A | Spin | [78] |

**Table 7.** Performances, areas, and perovskite preparation processes of reported high-efficiency all-inorganic perovskite solar cells.

| $E_g^{ip}$ [eV] | $V_{OC}$ [V] | $J_{SC}$ [mA cm$^{-2}$] | *FF* [%] | *η* [%] | Area [cm$^2$] | Preparation | Refs. |
|---|---|---|---|---|---|---|---|
| 1.70 | 1.198 | 20.59 | 82.5 | 20.37 | 0.094 | Spin | [130] |
| 1.71 | 1.148 | 20.76 | 84.3 | 20.08 | 0.09 | Spin | [131] |
| 1.72 | 1.23 | 19.94 | 80.11 | 19.65 | 0.09 | Spin | [74] |
| 1.70 | 1.244 | 20.6 | 82.52 | 21.15 | 0.09 | Spin | [66] |
| 1.69 | 1.22 | 20.64 | 82.1 | 20.67 | 0.09 | Spin | [132] |
| 1.70 | 1.229 | 20.51 | 83.3 | 20.98 | 0.09 | Spin | [67] |
| 1.69 | 1.17 | 20.6 | 83 | 20.01 | 0.09 | Blade | [133] |
| 1.71 | 1.233 | 20.55 | 81.9 | 20.8 | 0.09 | Spin | [73] |
| 1.70 | 1.2 | 20.58 | 82.87 | 20.5 | 0.09 | Spin | [134] |
| 1.68 | 1.24 | 20.3 | 81.23 | 20.47 | 0.09 | Spin | [135] |
| 1.72 | 1.26 | 20.71 | 83.8 | 21.86 | 0.064 | Spin | [65] |
| 1.70 | 1.22 | 21.72 | 81.5 | 21.59 | 0.09 | Spin + evaporation | [71] |
| 1.74 | 1.27 | 19.4 | 85.31 | 21.02 | 0.0737 | Spin | [69] |

**Table 8.** Performances of reported highly stable perovskite solar cells that can endure a 1000 h stability test.

| $E_g^{ip}$ [eV] | $V_{OC}$ [V] | $J_{SC}$ [mA cm$^{-2}$] | FF [%] | η [%] | η at 0 h [%] | η at 1000 h [%] | $E_{1000h}$ [Wh cm$^{-2}$] | Refs. |
|---|---|---|---|---|---|---|---|---|
| 1.53 | 1.16 | 25.74 | 80.2 | 23.9 | 22.9 | 23.4 | 23.3 | [12c] |
| 1.55 | 1.164 | 24.8 | 80.9 | 23.35 | 23.4 | 22.9 | 23.3 | [80a] |
| 1.53 | 1.15 | 26.2 | 82 | 24.7 | 23.8 | 22.6 | 22.8 | [80b] |
| 1.53 | 1.158 | 25.25 | 84.3 | 24.7 | 23.1 | 20.7 | 22.0 | [80c] |
| 1.55 | 1.15 | 24.33 | 78.65 | 22.01 | 22.0 | 20.6 | 21.2 | [80d] |

For perovskite cells, the active area (labeled with $^{ac}$ in the following tables) is normally used to determine the device area because the light illuminates from the TCO side, and there is no channel, finger electrode, or other shelter. In other words, no dead area was included in the measurements. Note that the active area is also the default device area for the data without any labels in the following tables. As for the modules, both the active area and aperture area (labeled with $^{ap}$) have been reported in the literature. Owing to the existence of a dead area (caused by lines P1, P2, and P3), the active area is smaller than the aperture area.[8b,39,56,57] For any other type of cells/module (such as GaAs, Si, CIGS, etc.), the total area (labeled with $^{t}$), aperture area, and designated area (labeled with $^{da}$) are used. The relationships between them have been well explained by Green et al.[87] The total area is the total projected area, including all the components and even the module frame. The aperture area generally excludes the frame but includes active layers, busbars, fingers, and interconnects,[87] while the designated area further excludes all or parts of the busbars, fingers, and interconnects. Masks are widely used to restrict illumination areas. The designated area was the same as the active area for most laboratory perovskite cells (**Tables** 3–8).

## Supporting Information

Supporting Information is available from the Wiley Online Library or from the author.

## Acknowledgements

The authors acknowledge funding by the Helmholtz Association via the POF IV funding (T.K.), via the Innovation Platform SolarTap, via the project “Beschleunigter Transfer der nächsten Generation von Solarzellen in die Massenfertigung – Zukunftstechnologie Tandem - Solarzellen” (T.K.), via the Helmholtz.AI project AISPA – AI-driven instantaneous solar cell property analysis (T.K.) as well as by the Deutsche Forschungsgemeinschaft (German Research Foundation) via the project “Correlating Defect Densities with Recombination Losses in Halide-Perovskite Solar Cells” (T.K.).

Open access funding enabled and organized by Projekt DEAL.

## Conflict of Interest

The authors declare no conflict of interest.

## Keywords

performance loss analysis, perovskite module, perovskite solar cells, preparation techniques, upscaling process

Received: August 19, 2024
Revised: October 26, 2024
Published online: November 20, 2024

---

[1] a) National Renewable Energy Laboratory (NREL), Best Research-Cell Efficiency Chart, https://www.nrel.gov/pv/cell-efficiency.html (accessed: November 2024); b) M. A. Green, E. D. Dunlop, M. Yoshita, N. Kopidakis, K. Bothe, G. Siefer, D. Hinken, M. Rauer, J. Hohl-Ebinger, X. Hao, *Prog. Photovoltaics* **2024**, *32*, 425; c) H. Chen, C. Liu, J. Xu, A. Maxwell, W. Zhou, Y. Yang, Q. Zhou, A. S. R. Bati, H. Wan, Z. Wang, L. Zeng, J. Wang, P. Serles, Y. Liu, S. Teale, Y. Liu, M. I. Saidaminov, M. Li, N. Rolston, S. Hoogland, T. Filleter, M. G. Kanatzidis, B. Chen, Z. Ning, E. H. Sargent, *Science* **2024**, *384*, 189.

[2] National Renewable Energy Laboratory (NREL), Champion Photovoltaic Module Efficiency Chart, https://www.nrel.gov/pv/module-efficiency.html (accessed: November 2024).

[3] J. Zhou, L. Tan, Y. Liu, H. Li, X. Liu, M. Li, S. Wang, Y. Zhang, C. Jiang, R. Hua, W. Tress, S. Meloni, C. Yi, *Joule* **2024**, *8*, 1691.

[4] a) B. Parida, A. Singh, A. K. Kalathil Soopy, S. Sangaraju, M. Sundaray, S. Mishra, S. Liu, A. Najar, *Adv. Sci.* **2022**, *9*, 2200308; b) Y. Wang, C. Duan, P. Lv, Z. Ku, J. Lu, F. Huang, Y.-B. Cheng, *Natl. Sci. Rev.* **2021**, *8*, nwab075; c) X. Luo, X. Lin, F. Gao, Y. Zhao, X. Li, L. Zhan, Z. Qiu, J. Wang, C. Chen, L. Meng, X. Gao, Y. Zhang, Z. Huang, R. Fan, H. Liu, Y. Chen, X. Ren, J. Tang, C.-H. Chen, D. Yang, Y. Tu, X. Liu, D. Liu, Q. Zhao, J. You, J. Fang, Y. Wu, H. Han, X. Zhang, D. Zhao, et al., *Sci. China: Chem.* **2022**, *65*, 2369.

[5] a) L. Gil-Escrig, M. Ross, J. Sutter, A. Al-Ashouri, C. Becker, S. Albrecht, *Sol. RRL* **2021**, *5*, 2000553; b) L. Mao, T. Yang, H. Zhang, J. H. Shi, Y. C. Hu, P. Zeng, F. M. Li, J. Gong, X. Y. Fang, Y. Q. Sun, X. C. Liu, J. L. Du, A. J. Han, L. P. Zhang, W. Z. Liu, F. Y. Meng, X. D. Cui, Z. X. Liu, M. Z. Liu, *Adv. Mater.* **2022**, *34*, 2206193.

[6] T. Abzieher, D. T. Moore, M. Roß, S. Albrecht, J. Silvia, H. Tan, Q. Jeangros, C. Ballif, M. T. Hoerantner, B.-S. Kim, H. J. Bolink, P. Pistor, J. C. Goldschmidt, Y.-H. Chiang, S. D. Stranks, J. Borchert, M. D. McGehee, M. Morales-Masis, J. B. Patel, A. Bruno, U. W. Paetzold, *Energy Environ. Sci.* **2024**, *17*, 1645.

[7] J. M. Kestner, S. McElvain, S. Kelly, T. R. Ohno, L. M. Woods, C. A. Wolden, *Sol. Energy Mater. Sol. Cells* **2004**, *83*, 55.

[8] a) H. Li, J. Zhou, L. Tan, M. Li, C. Jiang, S. Wang, X. Zhao, Y. Liu, Y. Zhang, Y. Ye, W. Tress, C. Yi, *Sci. Adv.* **2022**, *8*, 7422; b) T. Bu, L. K. Ono, J. Li, J. Su, G. Tong, W. Zhang, Y. Liu, J. Zhang, J. Chang, S. Kazaoui, F. Huang, Y.-B. Cheng, Y. Qi, *Nat. Energy* **2022**, *7*, 528; c) C. B. Fei, N. X. Li, M. R. Wang, X. M. Wang, H. Y. Gu, B. Chen, Z. Zhang, Z. Y. Ni, H. Y. Jiao, W. Z. Xu, Z. F. Shi, Y. F. Yan, J. S. Huang, *Science* **2023**, *380*, 823; d) W. Feng, J. Tao, G. Liu, G. Yang, J.-X. Zhong, Y. Fang, L. Gong, S. Yang, W.-Q. Wu, *Angew. Chem., Int. Ed.* **2023**, *62*, 202300265.

[9] S.-W. Lee, S. Bae, D. Kim, H.-S. Lee, *Adv. Mater.* **2020**, *32*, 2002202.

[10] a) D. Wang, M. Wright, N. K. Elumalai, A. Uddin, *Sol. Energy Mater. Sol. Cells* **2016**, *147*, 255; b) T. Leijtens, G. E. Eperon, N. K. Noel, S. N. Habisreutinger, A. Petrozza, H. J. Snaith, *Adv Energy Mater* **2015**, *5*, 1500963.

[11] a) H. Huang, M. I. Bodnarchuk, S. V. Kershaw, M. V. Kovalenko, A. L. Rogach, *ACS Energy Lett.* **2017**, *2*, 2071; b) Z. Li, M. Yang, J.-S. Park, S.-H. Wei, J. J. Berry, K. Zhu, *Chem. Mater.* **2016**, *28*, 284; c) C. J. Bartel, C. Sutton, B. R. Goldsmith, R. Ouyang, C. B. Musgrave, L. M. Ghiringhelli, M. Scheffler, *Sci. Adv.* **2019**, *5*, 0693; d) Q. Jiang, K. Zhu, *Nat. Rev. Mater.* **2024**, *9*, 399.

[12] a) K. Domanski, B. Roose, T. Matsui, M. Saliba, S.-H. Turren-Cruz, J.-P. Correa-Baena, C. R. Carmona, G. Richardson, J. M. Foster, F. De Angelis, J. M. Ball, A. Petrozza, N. Mine, M. K. Nazeeruddin, W. Tress, M. Grätzel, U. Steiner, A. Hagfeldt, A. Abate, *Energy Environ.*

*Sci.* **2017**, *10*, 604; b) S. Bai, P. Da, C. Li, Z. Wang, Z. Yuan, F. Fu, M. Kawecki, X. Liu, N. Sakai, J. T.-W. Wang, S. Huettner, S. Buecheler, M. Fahlman, F. Gao, H. J. Snaith, *Nature* **2019**, *571*, 245; c) C. Li, X. Wang, E. Bi, F. Jiang, S. M. Park, Y. Li, L. Chen, Z. Wang, L. Zeng, H. Chen, Y. Liu, C. R. Grice, A. Abudulimu, J. Chung, Y. Xian, T. Zhu, H. Lai, B. Chen, R. J. Ellingson, F. Fu, D. S. Ginger, Z. Song, E. H. Sargent, Y. Yan, *Science* **2023**, *379*, 690.

[13] a) M. Kulbak, S. Gupta, N. Kedem, I. Levine, T. Bendikov, G. Hodes, D. Cahen, *J. Phys. Chem. Lett.* **2016**, *7*, 167; b) W. Xiang, W. Tress, *Adv. Mater.* **2019**, *31*, 1902851.

[14] C. C. Boyd, R. Cheacharoen, T. Leijtens, M. D. McGehee, *Chem. Rev.* **2019**, *119*, 3418.

[15] a) L. N. Quan, M. Yuan, R. Comin, O. Voznyy, E. M. Beauregard, S. Hoogland, A. Buin, A. R. Kirmani, K. Zhao, A. Amassian, D. H. Kim, E. H. Sargent, *J. Am. Chem. Soc.* **2016**, *138*, 2649; b) L. Etgar, *Energy Environ. Sci.* **2018**, *11*, 234; c) Y. Zhang, N.-G. Park, *ACS Energy Lett.* **2022**, *7*, 757.

[16] L. Krückemeier, U. Rau, M. Stolterfoht, T. Kirchartz, *Adv. Energy Mater.* **2019**, *10*, 1902573.

[17] O. Almora, D. Baran, G. C. Bazan, C. I. Cabrera, S. Erten-Ela, K. Forberich, F. Guo, J. Hauch, A. W. Y. Ho-Baillie, T. J. Jacobsson, R. A. J. Janssen, T. Kirchartz, N. Kopidakis, M. A. Loi, R. R. Lunt, X. Mathew, M. D. McGehee, J. Min, D. B. Mitzi, M. K. Nazeeruddin, J. Nelson, A. F. Nogueira, U. W. Paetzold, B. P. Rand, U. Rau, H. J. Snaith, E. Unger, L. Vaillant-Roca, C. Yang, H.-L. Yip, et al., *Adv. Energy Mater.* **2023**, *13*, 2203313.

[18] a) J. F. Guillemoles, T. Kirchartz, D. Cahen, U. Rau, *Nat. Photonics* **2019**, *13*, 501; b) J.-F. Guillemoles, T. Kirchartz, D. Cahen, U. Rau, *Nat. Photonics* **2021**, *15*, 165; c) Y. Yuan, G. H. Yan, R. J. Hong, Z. C. Liang, T. Kirchartz, *Adv. Mater.* **2022**, *34*, 2108132.

[19] a) J. J. Yoo, G. Seo, M. R. Chua, T. G. Park, Y. Lu, F. Rotermund, Y.-K. Kim, C. S. Moon, N. J. Jeon, J.-P. Correa-Baena, V. Bulović, S. S. Shin, M. G. Bawendi, J. Seo, *Nature* **2021**, *590*, 587; b) M. A. Green, E. D. Dunlop, J. Hohl-Ebinger, M. Yoshita, N. Kopidakis, K. Bothe, D. Hinken, M. Rauer, X. Hao, *Prog. Photovoltaics* **2022**, *30*, 687; c) M. Kim, J. Jeong, H. Lu, T. K. Lee, F. T. Eickemeyer, Y. Liu, I. W. Choi, S. J. Choi, Y. Jo, H. B. Kim, S. I. Mo, Y. K. Kim, H. Lee, N. G. An, S. Cho, W. R. Tress, S. M. Zakeeruddin, A. Hagfeldt, J. Y. Kim, M. Gratzel, D. S. Kim, *Science* **2022**, *375*, 302; d) Z. Li, B. Li, X. Wu, S. A. Sheppard, S. Zhang, D. Gao, N. J. Long, Z. Zhu, *Science* **2022**, *376*, 416; e) X. Luo, Z. Shen, Y. Shen, Z. Su, X. Gao, Y. Wang, Q. Han, L. Han, *Adv. Mater.* **2022**, *34*, 2202100; f) T. Zhang, F. Wang, H.-B. Kim, I.-W. Choi, C. Wang, E. Cho, R. Konefal, Y. Puttisong, K. Terado, L. Kobera, M. Chen, M. Yang, S. Bai, B. Yang, J. Suo, S.-C. Yang, X. Liu, F. Fu, H. Yoshida, W. M. Chen, J. Brus, V. Coropceanu, A. Hagfeldt, J.-L. Brédas, M. Fahlman, D. S. Kim, Z. Hu, F. Gao, *Science* **2022**, *377*, 495501; g) J. Park, J. Kim, H. S. Yun, M. J. Paik, E. Noh, H. J. Mun, M. G. Kim, T. J. Shin, S. I. Seok, *Nature* **2023**, *616*, 724.

[20] M. Roß, L. Gil-Escrig, A. Al-Ashouri, P. Tockhorn, M. Jošt, B. Rech, S. Albrecht, *ACS Appl. Mater. Interfaces* **2020**, *12*, 39261.

[21] M. Du, S. Zhao, L. Duan, Y. Cao, H. Wang, Y. Sun, L. Wang, X. Zhu, J. Feng, L. Liu, X. Jiang, Q. Dong, Y. Shi, K. Wang, S. Liu, *Joule* **2022**, *6*, 1931.

[22] Y. Kang, R. Li, A. Wang, J. Kang, Z. Wang, W. Bi, Y. Yang, Y. Song, Q. Dong, *Energy Environ. Sci.* **2022**, *15*, 3439.

[23] H. Eggers, F. Schackmar, T. Abzieher, Q. Sun, U. Lemmer, Y. Vaynzof, B. S. Richards, G. Hernandez-Sosa, U. W. Paetzold, *Adv. Energy Mater.* **2020**, *10*, 1903184.

[24] C. Chen, J. Chen, H. Han, L. Chao, J. Hu, T. Niu, H. Dong, S. Yang, Y. Xia, Y. Chen, W. Huang, *Nature* **2022**, *612*, 266.

[25] T. Thornber, O. S. Game, E. J. Cassella, M. E. O'Kane, J. E. Bishop, T. J. Routledge, T. I. Alanazi, M. Togay, P. J. M. Isherwood, L. C. Infante-Ortega, D. B. Hammond, J. M. Walls, D. G. Lidzey, *ACS Appl. Mater. Interfaces* **2022**, *14*, 37587.

[26] C. Dreessen, K. P. S. Zanoni, L. Gil-Escrig, N. Rodkey, J. I. Khan, F. Laquai, M. Sessolo, C. Roldán-Carmona, H. J. Bolink, *Adv. Opt. Mater.* **2024**, *12*, 2301019.

[27] a) P. Chen, Y. Xiao, S. D. Li, X. H. Jia, D. Y. Luo, W. Zhang, H. J. Snaith, Q. H. Gong, R. Zhu, *Chem. Rev.* **2024**, *124*, 10623; b) F. H. Isikgor, S. Zhumagali, L. V. T. Merino, M. De Bastiani, I. McCulloch, S. De Wolf, *Nat. Rev. Mater.* **2023**, *8*, 89.

[28] a) X. Y. Tong, L. S. Xie, J. Li, Z. W. Pu, S. Y. Du, M. J. Yang, Y. Y. Gao, M. Z. He, S. H. Wu, Y. H. Mai, Z. Y. Ge, *Adv. Mater.* **2024**, *36*, 2407032; b) N. Ren, L. Tan, M. Li, J. Zhou, Y. Ye, B. Jiao, L. Ding, C. Yi, *iEnergy* **2024**, *3*, 39.

[29] Q. Jiang, J. Tong, Y. Xian, R. A. Kerner, S. P. Dunfield, C. Xiao, R. A. Scheidt, D. Kuciauskas, X. Wang, M. P. Hautzinger, R. Tirawat, M. C. Beard, D. P. Fenning, J. J. Berry, B. W. Larson, Y. Yan, K. Zhu, *Nature* **2022**, *611*, 278.

[30] J. S. Feng, Y. X. Jiao, H. Wang, X. J. Zhu, Y. M. Sun, M. Y. Du, Y. X. Cao, D. Yang, S. Z. Liu, *Energy Environ. Sci.* **2021**, *14*, 3035.

[31] H. Li, L. G. Tan, C. F. Jiang, M. H. Li, J. J. Zhou, Y. R. Ye, Y. Liu, C. Y. Yi, *Adv. Funct. Mater.* **2023**, *33*, 2211232.

[32] a) M. Kim, G. H. Kim, T. K. Lee, I. W. Choi, H. W. Choi, Y. Jo, Y. J. Yoon, J. W. Kim, J. Lee, D. Huh, H. Lee, S. K. Kwak, J. Y. Kim, D. S. Kim, *Joule* **2019**, *3*, 2179; b) W. Chen, Y. C. Zhou, G. C. Chen, Y. H. Wu, B. Tu, F. Z. Liu, L. Huang, A. M. C. Ng, A. B. Djurisic, Z. B. He, *Adv. Energy Mater.* **2019**, *9*, 1803872; c) M. M. Tavakoli, P. Yadav, D. Prochowicz, M. Sponseller, A. Osherov, V. Bulovic, J. Kong, *Adv. Energy Mater.* **2019**, *9*, 1803587.

[33] Y. Zhao, F. Ma, Z. Qu, S. Yu, T. Shen, H. X. Deng, X. Chu, X. Peng, Y. Yuan, X. Zhang, J. You, *Science* **2022**, *377*, 531.

[34] W. Peng, K. Mao, F. Cai, H. Meng, Z. Zhu, T. Li, S. Yuan, Z. Xu, X. Feng, J. Xu, M. D. McGehee, J. Xu, *Science* **2023**, *379*, 683.

[35] Y. H. Chiang, M. Anaya, S. D. Stranks, *ACS Energy Lett* **2020**, *5*, 2498.

[36] J. Li, H. A. Dewi, H. Wang, J. H. Lew, N. Mathews, S. Mhaisalkar, A. Bruno, *Sol. RRL* **2020**, *4*, 2000473.

[37] K. B. Lohmann, J. B. Patel, M. U. Rothmann, C. Q. Xia, R. D. J. Oliver, L. M. Herz, H. J. Snaith, M. B. Johnston, *ACS Energy Lett.* **2020**, *5*, 710.

[38] S. Akel, A. Kulkarni, U. Rau, T. Kirchartz, *PRX Energy* **2023**, *2*, 013004.

[39] S. Chen, X. Dai, S. Xu, H. Jiao, L. Zhao, J. Huang, *Science* **2021**, *373*, 902.

[40] Y. H. Deng, Q. F. Dong, C. Bi, Y. B. Yuan, J. S. Huang, *Adv. Energy Mater.* **2016**, *6*, 1600372.

[41] a) Z. Ren, K. Liu, H. Hu, X. Guo, Y. Gao, P. W. K. Fong, Q. Liang, H. Tang, J. Huang, H. Zhang, M. Qin, L. Cui, H. T. Chandran, D. Shen, M. F. Lo, A. Ng, C. Surya, M. Shao, C. S. Lee, X. Lu, F. Laquai, Y. Zhu, G. Li, *Light: Sci. Appl.* **2021**, *10*, 239; b) W. Q. Wu, P. N. Rudd, Q. Wang, Z. Yang, J. Huang, *Adv. Mater.* **2020**, *32*, 2000995; c) W. Q. Wu, Z. Yang, P. N. Rudd, Y. Shao, X. Dai, H. Wei, J. Zhao, Y. Fang, Q. Wang, Y. Liu, Y. Deng, X. Xiao, Y. Feng, J. Huang, *Sci. Adv.* **2019**, *5*, 8925.

[42] Q. Liang, K. Liu, M. Sun, Z. Ren, P. W. K. Fong, J. Huang, M. Qin, Z. Wu, D. Shen, C. S. Lee, J. Hao, X. Lu, B. Huang, G. Li, *Adv. Mater.* **2022**, *34*, 2200276.

[43] S. Chen, X. Xiao, H. Gu, J. Huang, *Sci. Adv.* **2021**, *7*, eabe8130.

[44] L. E. Mundt, W. Kwapil, M. A. Yakoob, J. P. Herterich, M. Kohlstädt, U. Würfel, M. C. Schubert, S. W. Glunz, *IEEE J. Photovoltaics* **2019**, *9*, 452.

[45] Y. Deng, Q. Wang, Y. Yuan, J. Huang, *Mater. Horiz.* **2015**, *2*, 578.

[46] M. Golubitsky, J. W. Swift, E. Knobloch, *Phys. D* **1984**, *10*, 249.

[47] a) S. W. Hong, J. Xu, J. Xia, Z. Lin, F. Qiu, Y. Yang, *Chem. Mater.* **2005**, *17*, 6223; b) R. D. Deegan, O. Bakajin, T. F. Dupont, G. Huber, S. R. Nagel, T. A. Witten, *Nature* **1997**, *389*, 827.

[48] M. Wang, C. Fei, M. A. Uddin, J. Huang, *Sci. Adv.* **2022**, *8*, 5977.

[49] S. S. Chen, X. Xiao, B. Chen, L. L. Kelly, J. J. Zhao, Y. Z. Lin, M. F. Toney, J. S. Huang, *Sci. Adv.* **2021**, *7*, eabb2412.

[50] A. S. Subbiah, F. H. Isikgor, C. T. Howells, M. De Bastiani, J. Liu, E. Aydin, F. Furlan, T. G. Allen, F. Xu, S. Zhumagali, S. Hoogland, E. H. Sargent, I. McCulloch, S. De Wolf, *ACS Energy Lett.* **2020**, *5*, 3034.
[51] S.-H. Turren-Cruz, A. Hagfeldt, M. Saliba, *Science* **2018**, *362*, 449.
[52] M. Du, X. Zhu, L. Wang, H. Wang, J. Feng, X. Jiang, Y. Cao, Y. Sun, L. Duan, Y. Jiao, K. Wang, X. Ren, Z. Yan, S. Pang, S. Liu, *Adv. Mater.* **2020**, *32*, 2004979.
[53] F. Xu, J. Liu, A. S. Subbiah, W. Liu, J. Kang, G. T. Harrison, X. Yang, F. H. Isikgor, E. Aydin, M. De Bastiani, S. De Wolf, *Small Sci.* **2021**, *1*, 2000044.
[54] J. Li, J. Dagar, O. Shargaieva, M. A. Flatken, H. Köbler, M. Fenske, C. Schultz, B. Stegemann, J. Just, D. M. Többens, A. Abate, R. Munir, E. Unger, *Adv. Energy Mater.* **2021**, *11*, 2003460.
[55] a) X. Dai, S. Chen, Y. Deng, A. Wood, G. Yang, C. Fei, J. Huang, *PRX Energy* **2022**, *1*, 013004; b) V. Bermudez, A. Perez-Rodriguez, *Nat. Energy* **2018**, *3*, 466; c) M. Zinßer, T. Helder, T. Magorian Friedlmeier, A. Bauer, T. Kirchartz, U. Rau, R. Wächter, M. Powalla, *Commun. Phys.* **2023**, *6*, 55.
[56] I. Zimmermann, M. Provost, S. Mejaouri, M. Al Atem, A. Blaizot, A. Duchatelet, S. Collin, J. Rousset, *ACS Appl. Mater. Interfaces* **2022**, *14*, 11636.
[57] J. Zhu, S. Park, O. Y. Gong, C. Sohn, Z. Li, Z. Zhang, B. Jo, W. Kim, G. S. Han, D. H. Kim, T. K. Ahn, J. Lee, H. S. Jung, *Energy Environ. Sci.* **2021**, *14*, 4903.
[58] T. Abzieher, J. A. Schwenzer, S. Moghadamzadeh, F. Sutterlüti, I. M. Hossain, M. Pfau, E. Lotter, M. Hetterich, B. S. Richards, U. Lemmer, M. Powalla, U. W. Paetzold, *IEEE J. Photovoltaics* **2019**, *9*, 1249.
[59] M. Kim, J. Jeong, H. Lu, T. K. Lee, F. T. Eickemeyer, Y. Liu, I. W. Choi, S. J. Choi, Y. Jo, H.-B. Kim, S.-I. Mo, Y.-K. Kim, H. Lee, N. G. An, S. Cho, W. R. Tress, S. M. Zakeeruddin, A. Hagfeldt, J. Y. Kim, M. Grätzel, D. S. Kim, *Science* **2022**, *375*, 302.
[60] J. Li, H. Wang, X. Y. Chin, H. A. Dewi, K. Vergeer, T. W. Goh, J. W. M. Lim, J. H. Lew, K. P. Loh, C. Soci, T. C. Sum, H. J. Bolink, N. Mathews, S. Mhaisalkar, A. Bruno, *Joule* **2020**, *4*, 1035.
[61] Y. Y. Kim, T.-Y. Yang, R. Suhonen, A. Kemppainen, K. Hwang, N. J. Jeon, J. Seo, *Nat. Commun.* **2020**, *11*, 5146.
[62] K. J. Prince, H. M. Mirletz, E. A. Gaulding, L. M. Wheeler, R. A. Kerner, X. Zheng, L. T. Schelhas, P. Tracy, C. A. Wolden, J. J. Berry, S. Ovaitt, T. M. Barnes, J. M. Luther, *Nat. Mater.* **2024**.
[63] I. M. Peters, J. Hauch, C. Brabec, P. Sinha, *Joule* **2021**, *5*, 3137.
[64] a) L. Shi, M. P. Bucknall, T. L. Young, M. Zhang, L. Hu, J. Bing, D. S. Lee, J. Kim, T. Wu, N. Takamure, D. R. McKenzie, S. Huang, M. A. Green, A. W. Y. Ho-Baillie, *Science* **2020**, *368*, 2412; b) A. Mei, Y. Sheng, Y. Ming, Y. Hu, Y. Rong, W. Zhang, S. Luo, G. Na, C. Tian, X. Hou, Y. Xiong, Z. Zhang, S. Liu, S. Uchida, T.-W. Kim, Y. Yuan, L. Zhang, Y. Zhou, H. Han, *Joule* **2020**, *4*, 2646.
[65] J. Qiu, X. Mei, M. Zhang, G. Wang, S. Zou, L. Wen, J. Huang, Y. Hua, X. Zhang, *Angew. Chem., Int. Ed.* **2024**, *63*, 202401751.
[66] J. Wang, Y. Che, Y. Duan, Z. Liu, S. Yang, D. Xu, Z. Fang, X. Lei, Y. Li, S. Liu, *Adv. Mater.* **2023**, *35*, 2210223.
[67] C. Xu, S. Zhang, W. Fan, F. Cheng, H. Sun, Z. Kang, Y. Zhang, *Adv. Mater.* **2023**, *35*, 2207172.
[68] a) Y. Huang, W. J. Yin, Y. He, *J. Phys. Chem. C* **2018**, *122*, 1345; b) Y. F. Li, C. H. Zhang, X. X. Zhang, D. Huang, Q. Shen, Y. C. Cheng, W. Huang, *Appl. Phys. Lett.* **2017**, *111*, 162106.
[69] X. Chu, Q. Ye, Z. Wang, C. Zhang, F. Ma, Z. Qu, Y. Zhao, Z. Yin, H.-X. Deng, X. Zhang, J. You, *Nat. Energy* **2023**, *8*, 372.
[70] Y. Chen, X. Liu, Y. Zhao, *Angew. Chem., Int. Ed.* **2022**, *61*, 202110603.
[71] S. S. Mali, J. V. Patil, J.-Y. Shao, Y.-W. Zhong, S. R. Rondiya, N. Y. Dzade, C. K. Hong, *Nat. Energy* **2023**, *8*, 989.
[72] Y. Wang, X. Liu, T. Zhang, X. Wang, M. Kan, J. Shi, Y. Zhao, *Angew. Chem., Int. Ed.* **2019**, *58*, 16691.
[73] X. Gu, W. Xiang, Q. Tian, S. Liu, *Angew. Chem., Int. Ed.* **2021**, *60*, 23164.
[74] K. Wang, C. Gao, Z. Xu, Q. Tian, X. Gu, L. Zhang, S. Zhang, K. Zhao, S. Liu, *Adv. Funct. Mater.* **2021**, *31*, 2101568.
[75] a) Y. Fu, W. Zheng, X. Wang, M. P. Hautzinger, D. Pan, L. Dang, J. C. Wright, A. Pan, S. Jin, *J. Am. Chem. Soc.* **2018**, *140*, 15675; b) G. Grancini, M. K. Nazeeruddin, *Nat. Rev. Mater.* **2019**, *4*, 4.
[76] M. Shao, T. Bie, L. Yang, Y. Gao, X. Jin, F. He, N. Zheng, Y. Yu, X. Zhang, *Adv. Mater.* **2022**, *34*, 2107211.
[77] Z. Xing, B. Fan, X. Meng, D. Li, Z. Huang, L. Li, Y. Zhang, F. Wang, X. Hu, T. Hu, T. Riedl, Y. Chen, *Energy Environ. Sci.* **2024**, *17*, 3660.
[78] Y. Wang, D. Li, Z. Xing, J. Li, X. Hu, T. Hu, Y. Chen, *Adv. Funct. Mater.* **2024**, *34*, 2401203.
[79] S. Wang, Y. Liu, J. Zou, J. Jin, Y. Jiang, T. Zeng, W. Zhao, R.-X. He, B. Chen, Y. Chen, S. Jin, H.-X. Li, Z. Xie, C.-A. Wang, W. Sun, Q. Cao, X.-Z. Zhao, *InfoMat* **2023**, *5*, 12396.
[80] a) D. Gao, B. Li, Z. Li, X. Wu, S. Zhang, D. Zhao, X. Jiang, C. Zhang, Y. Wang, Z. Li, N. Li, S. Xiao, W. C. H. Choy, A. K.-Y. Jen, S. Yang, Z. Zhu, *Adv. Mater.* **2023**, *35*, 2206387; b) P. Shi, Y. Ding, B. Ding, Q. Xing, T. Kodalle, C. M. Sutter-Fella, I. Yavuz, C. Yao, W. Fan, J. Xu, Y. Tian, D. Gu, K. Zhao, S. Tan, X. Zhang, L. Yao, P. J. Dyson, J. L. Slack, D. Yang, J. Xue, M. K. Nazeeruddin, Y. Yang, R. Wang, *Nature* **2023**, *620*, 323; c) F. Zhang, S. Y. Park, C. Yao, H. Lu, S. P. Dunfield, C. Xiao, S. Uličná, X. Zhao, L. Du Hill, X. Chen, X. Wang, L. E. Mundt, K. H. Stone, L. T. Schelhas, G. Teeter, S. Parkin, E. L. Ratcliff, Y.-L. Loo, J. J. Berry, M. C. Beard, Y. Yan, B. W. Larson, K. Zhu, *Science* **2022**, *375*, 71; d) T. N. Mandal, J. H. Heo, S. H. Im, W.-S. Kim, *Sol. RRL* **2023**, *7*, 2300496.
[81] a) L.-L. Gao, C.-X. Li, C.-J. Li, G.-J. Yang, *J. Mater. Chem. A* **2017**, *5*, 1548; b) R. Patidar, D. Burkitt, K. Hooper, D. Richards, T. Watson, *Mater. Today Commun.* **2020**, *22*, 100808; c) J.-W. Lee, D.-K. Lee, D.-N. Jeong, N.-G. Park, *Adv. Funct. Mater.* **2019**, *29*, 1807047.
[82] Y. Wang, S. Akel, B. Klingebiel, T. Kirchartz, *Adv. Energy Mater.* **2024**, *14*, 2302614.
[83] J. Peng, D. Walter, Y. Ren, M. Tebyetekerwa, Y. Wu, T. Duong, Q. Lin, J. Li, T. Lu, M. A. Mahmud, O. L. C. Lem, S. Zhao, W. Liu, Y. Liu, H. Shen, L. Li, F. Kremer, H. T. Nguyen, D.-Y. Choi, K. J. Weber, K. R. Catchpole, T. P. White, *Science* **2021**, *371*, 390.
[84] J. Peng, F. Kremer, D. Walter, Y. Wu, Y. Ji, J. Xiang, W. Liu, T. Duong, H. Shen, T. Lu, F. Brink, D. Zhong, L. Li, O. Lee Cheong Lem, Y. Liu, K. J. Weber, T. P. White, K. R. Catchpole, *Nature* **2022**, *601*, 573.
[85] S. Yu, Z. Xiong, H. Zhou, Q. Zhang, Z. Wang, F. Ma, Z. Qu, Y. Zhao, X. Chu, X. Zhang, J. You, *Science* **2023**, *382*, 1399.
[86] C.-H. Chiang, C.-G. Wu, *ACS Nano* **2018**, *12*, 10355.
[87] M. A. Green, E. D. Dunlop, G. Siefer, M. Yoshita, N. Kopidakis, K. Bothe, X. Hao, *Prog. Photovoltaics* **2023**, *31*, 3.
[88] M. A. Green, Y. Hishikawa, E. D. Dunlop, D. H. Levi, J. Hohl-Ebinger, M. Yoshita, A. W. Y. Ho-Baillie, *Prog. Photovoltaics* **2019**, *27*, 3.
[89] M. A. Green, E. D. Dunlop, D. H. Levi, J. Hohl-Ebinger, M. Yoshita, A. W. Y. Ho-Baillie, *Prog. Photovoltaics* **2019**, *27*, 565.
[90] M. A. Green, E. D. Dunlop, M. Yoshita, N. Kopidakis, K. Bothe, G. Siefer, X. Hao, *Prog. Photovoltaics* **2024**, *32*, 3.
[91] L. Zhu, M. Zhang, J. Xu, C. Li, J. Yan, G. Zhou, W. Zhong, T. Hao, J. Song, X. Xue, Z. Zhou, R. Zeng, H. Zhu, C.-C. Chen, R. C. I. MacKenzie, Y. Zou, J. Nelson, Y. Zhang, Y. Sun, F. Liu, *Nat. Mater.* **2022**, *21*, 656.
[92] M. A. Green, Y. Hishikawa, E. D. Dunlop, D. H. Levi, J. Hohl-Ebinger, A. W. Y. Ho-Baillie, *Prog. Photovoltaics* **2018**, *26*, 3.
[93] M. A. Green, Y. Hishikawa, W. Warta, E. D. Dunlop, D. H. Levi, J. Hohl-Ebinger, A. W. H. Ho-Baillie, *Prog. Photovoltaics* **2017**, *25*, 668.
[94] M. A. Green, E. D. Dunlop, M. Yoshita, N. Kopidakis, K. Bothe, G. Siefer, X. Hao, *Prog. Photovoltaics* **2023**, *31*, 651.
[95] S. Liu, J. Li, W. Xiao, R. Chen, Z. Sun, Y. Zhang, X. Lei, S. Hu, M. Kober-Czerny, J. Wang, F. Ren, Q. Zhou, H. Raza, Y. Gao, Y. Ji, S. Li,

H. Li, L. Qiu, W. Huang, Y. Zhao, B. Xu, Z. Liu, H. J. Snaith, N.-G. Park, W. Chen, *Nature* **2024**, *632*, 536.

[96] M. Green, E. Dunlop, J. Hohl-Ebinger, M. Yoshita, N. Kopidakis, X. Hao, *Prog. Photovoltaics* **2021**, *29*, 3.

[97] Y. Wang, T. Wu, J. Barbaud, W. Kong, D. Cui, H. Chen, X. Yang, L. Han, *Science* **2019**, *365*, 687.

[98] M. A. Green, E. D. Dunlop, J. Hohl-Ebinger, M. Yoshita, N. Kopidakis, X. Hao, *Prog. Photovoltaics* **2021**, *29*, 657.

[99] H. Su, X. Lin, Y. Wang, X. Liu, Z. Qin, Q. Shi, Q. Han, Y. Zhang, L. Han, *Sci. China: Chem.* **2022**, *65*, 1321.

[100] W. Chen, S. Liu, Q. Li, Q. Cheng, B. He, Z. Hu, Y. Shen, H. Chen, G. Xu, X. Ou, H. Yang, J. Xi, Y. Li, Y. Li, *Adv. Mater.* **2022**, *34*, 2110482.

[101] N. Li, X. Niu, L. Li, H. Wang, Z. Huang, Y. Zhang, Y. Chen, X. Zhang, C. Zhu, H. Zai, Y. Bai, S. Ma, H. Liu, X. Liu, Z. Guo, G. Liu, R. Fan, H. Chen, J. Wang, Y. Lun, X. Wang, J. Hong, H. Xie, D. S. Jakob, X. G. Xu, Q. Chen, H. Zhou, *Science* **2021**, *373*, 561.

[102] Z. Shen, Q. Han, X. Luo, Y. Shen, T. Wang, C. Zhang, Y. Wang, H. Chen, X. Yang, Y. Zhang, L. Han, *Energy Environ. Sci.* **2022**, *15*, 1078.

[103] Z. Fang, L. Wang, X. Mu, B. Chen, Q. Xiong, W. D. Wang, J. Ding, P. Gao, Y. Wu, J. Cao, *J. Am. Chem. Soc.* **2021**, *143*, 18989.

[104] M. Roß, S. Severin, M. B. Stutz, P. Wagner, H. Köbler, M. Favin-Lévêque, A. Al-Ashouri, P. Korb, P. Tockhorn, A. Abate, B. Stannowski, B. Rech, S. Albrecht, *Adv. Energy Mater.* **2021**, *11*, 2101460.

[105] J. Zhuang, C. Liu, B. Kang, H. Cheng, M. Xiao, L. Li, F. Yan, *Adv. Mater.* **2024**, *36*, 2309869.

[106] M. He, B. Li, X. Cui, B. Jiang, Y. He, Y. Chen, D. O'Neil, P. Szymanski, M. A. Ei-Sayed, J. Huang, Z. Lin, *Nat. Commun.* **2017**, *8*, 16045.

[107] W.-Q. Wu, P. N. Rudd, Z. Ni, C. H. Van Brackle, H. Wei, Q. Wang, B. R. Ecker, Y. Gao, J. Huang, *J. Am. Chem. Soc.* **2020**, *142*, 3989.

[108] R. He, S. Nie, X. Huang, Y. Wu, R. Chen, J. Yin, B. Wu, J. Li, N. Zheng, *Sol. RRL* **2021**, *6*, 2100639.

[109] Z. Yang, W. Zhang, S. Wu, H. Zhu, Z. Liu, Z. Liu, Z. Jiang, R. Chen, J. Zhou, Q. Lu, Z. Xiao, L. Shi, H. Chen, L. K. Ono, S. Zhang, Y. Zhang, Y. Qi, L. Han, W. Chen, *Sci. Adv.* **2021**, *7*, 3749.

[110] K. Xu, A. Al-Ashouri, Z.-W. Peng, E. Köhnen, H. Hempel, F. Akhundova, J. A. Marquez, P. Tockhorn, O. Shargaieva, F. Ruske, J. Zhang, J. Dagar, B. Stannowski, T. Unold, D. Abou-Ras, E. Unger, L. Korte, S. Albrecht, *ACS Energy Lett.* **2022**, *7*, 3600.

[111] I. Zimmermann, M. Al Atem, O. Fournier, S. Bernard, S. Jutteau, L. Lombez, J. Rousset, *Adv. Mater. Interfaces* **2021**, *8*, 2100743.

[112] M. Xu, W. Ji, Y. Sheng, Y. Wu, H. Cheng, J. Meng, Z. Yan, J. Xu, A. Mei, Y. Hu, Y. Rong, H. Han, *Nano Energy* **2020**, *74*, 104842.

[113] S. Chen, L. Zhang, L. Yan, X. Xiang, X. Zhao, S. Yang, B. Xu, *Adv. Funct. Mater.* **2019**, *29*, 1905487.

[114] Z. Li, P. Li, G. Chen, Y. Cheng, X. Pi, X. Yu, D. Yang, L. Han, Y. Zhang, Y. Song, *ACS Appl. Mater. Interfaces* **2020**, *12*, 39082.

[115] T. Abzieher, S. Moghadamzadeh, F. Schackmar, H. Eggers, F. Sutterlüti, A. Farooq, D. Kojda, K. Habicht, R. Schmager, A. Mertens, R. Azmi, L. Klohr, J. A. Schwenzer, M. Hetterich, U. Lemmer, B. S. Richards, M. Powalla, U. W. Paetzold, *Adv. Energy Mater.* **2019**, *9*, 1802995.

[116] C. Gao, P. Wang, H. Wang, C. Yu, B. Du, H. Zhang, T. Li, D. Liu, T. Wang, *ACS Appl. Energy Mater.* **2021**, *4*, 11496.

[117] J. E. Bishop, C. D. Read, J. A. Smith, T. J. Routledge, D. G. Lidzey, *Sci. Rep.* **2020**, *10*, 6610.

[118] C. Gao, H. Wang, P. Wang, J. L. Cai, Y. D. Sun, C. Yu, T. Li, X. S. Zhang, D. Liu, T. Wang, *J. Semicond.* **2022**, *43*, 092201.

[119] G. Juska, N. Nekrasas, K. Genevicius, *J. Non-Cryst. Solids* **2012**, *358*, 748.

[120] S. Sanden, O. Sandberg, Q. Xu, J. H. Smatt, G. Juska, M. Linden, R. Osterbacka, *Phys. Chem. Chem. Phys.* **2012**, *14*, 14186.

[121] C. Worsley, D. Raptis, S. M. P. Meroni, R. Patidar, A. Pockett, T. Dunlop, S. J. Potts, R. Bolton, C. M. E. Charbonneau, M. Carnie, E. Jewell, T. Watson, *Mater. Adv.* **2022**, *3*, 1125.

[122] S. Zhang, F. Y. Ye, X. Y. Wang, R. Chen, H. D. Zhang, L. Q. Zhan, X. Y. Jiang, Y. W. Li, X. Y. Ji, S. J. Liu, M. J. Yu, F. R. Yu, Y. L. Zhang, R. H. Wu, Z. H. Liu, Z. J. Ning, D. Neher, L. Y. Han, Y. Z. Lin, H. Tian, W. Chen, M. Stolterfoht, L. J. Zhang, W. H. Zhu, Y. Z. Wu, *Science* **2023**, *380*, 404.

[123] Y. Y. Wu, G. Y. Xu, Y. X. Shen, X. X. Wu, X. H. Tang, C. S. Han, Y. J. Chen, F. Yang, H. Y. Chen, Y. W. Li, Y. F. Li, *Adv. Mater.* **2024**, *36*, 2403531.

[124] L. S. Xie, S. Y. Du, J. Li, C. Liu, Z. W. Pu, X. Y. Tong, J. Liu, Y. H. Wang, Y. Y. Meng, M. J. Yang, W. Li, Z. Y. Ge, *Energy Environ. Sci.* **2023**, *16*, 5423.

[125] H. Ren, S. Yu, L. Chao, Y. Xia, Y. Sun, S. Zuo, F. Li, T. Niu, Y. Yang, H. Ju, B. Li, H. Du, X. Gao, J. Zhang, J. Wang, L. Zhang, Y. Chen, W. Huang, *Nat. Photonics* **2020**, *14*, 154.

[126] T. Luo, Y. Zhang, Z. Xu, T. Niu, J. Wen, J. Lu, S. Jin, S. Liu, K. Zhao, *Adv. Mater.* **2019**, *31*, 1903848.

[127] R. Yang, R. Li, Y. Cao, Y. Wei, Y. Miao, W. L. Tan, X. Jiao, H. Chen, L. Zhang, Q. Chen, H. Zhang, W. Zou, Y. Wang, M. Yang, C. Yi, N. Wang, F. Gao, C. R. McNeill, T. Qin, J. Wang, W. Huang, *Adv. Mater.* **2018**, *30*, 1804771.

[128] B. Wang, Q. Cheng, G. Huang, Y. Yue, W. Zhang, X. Li, Y. Li, W. Du, X. Liu, H. Zhang, Y. Zhang, H. Zhou, *Adv. Mater.* **2023**, *35*, 2207345.

[129] L. Jin, N. Ren, P. Wang, R. Li, Q. Xue, F. Huang, X. Zhang, Y. Zhao, X. Zhang, *Small* **2023**, *19*, 2205088.

[130] S. M. Yoon, H. Min, J. B. Kim, G. Kim, K. S. Lee, S. I. Seok, *Joule* **2021**, *5*, 183.

[131] B. Yu, J. Shi, S. Tan, Y. Cui, W. Zhao, H. Wu, Y. Luo, D. Li, Q. Meng, *Angew. Chem., Int. Ed.* **2021**, *60*, 13436.

[132] H. Zou, Y. Duan, S. Yang, D. Xu, L. Yang, J. Cui, H. Zhou, M. Wu, J. Wang, X. Lei, N. Zhang, Z. Liu, *Small* **2023**, *19*, 2206205.

[133] Y. Du, Q. Tian, X. Chang, J. Fang, X. Gu, X. He, X. Ren, K. Zhao, S. Liu, *Adv. Mater.* **2022**, *34*, 2106750.

[134] J. Zhang, B. Che, W. Zhao, Y. Fang, R. Han, Y. Yang, J. Liu, T. Yang, T. Chen, N. Yuan, J. Ding, S. Liu, *Adv. Mater.* **2022**, *34*, 2202735.

[135] Y. Che, Z. Liu, Y. Duan, J. Wang, S. Yang, D. Xu, W. Xiang, T. Wang, N. Yuan, J. Ding, S. Liu, *Angew. Chem., Int. Ed.* **2022**, *61*, 202205012.

**Genghua Yan** recieved her Ph.D. in materials physics and chemistry in 2018 from Sun Yat-sen University (SYSU). She has been working as a postdoctoral researcher at Forschungszentrum Jülich (FZJ) since 2021. Previously she did postdoctoral research at Jinan University. Her current research interests include the development and characterization of novel thin film materials and photoelectric devices.

**Ye Yuan** is currently working in the Institute of Energy Materials and Devices at the Forschungszentrum Jülich (FZJ) as a postdoctoral researcher. He received his doctoral degree of engineering in 2018 from Sun Yat-sen University (SYSU). Before that, he received his Bachelor's degree of science in 2013 from SYSU as well. He focuses on fundamental and experimental research in photovoltaics. His current research interests mainly include carrier dynamics, solar cell loss mechanism, and luminescence spectroscopy.

**Thomas Kirchartz** is a professor in the Department of Electrical Engineering and Information Technology at the University Duisburg-Essen (since 2013). In addition, he is the head of the Department of Analytics and Simulation and the group for Organic and Hybrid Solar Cells at the Research Centre Jülich (Institute of Energy Materials and Devices). Previously he was a junior research fellow at Imperial College London (2010–2013) and received a Dr.-Ing. from RWTH Aachen (2009). His research interests include the fundamental understanding of photovoltaic devices, their characterization and simulation, and the development of solution-processable solar cells.